5-2013

Bombardment of Graphite and Amorphous Carbon Surfaces Using Molecular Dynamics Simulations: Toward A More Realistic Experimental Model

Marcel Fallet
Clemson University, marcelfallet@gmail.com

Bombardment of Graphite and Amorphous Carbon Surfaces Using Molecular Dynamics Simulations: Toward A More Realistic Experimental Model

---

A Dissertation
Presented to
the Graduate School of
Clemson University

In Partial Fulfillment
of the Requirements for the Degree
Doctor of Philosophy
Chemistry

---

by
Marcel Fallet
May 2013

Accepted by:
Dr. Steven Stuart, Committee Chair
Dr. Brian Dominy
Dr. Jason McNeil
Dr. David Bruce

Abstract

Molecular dynamics (MD) simulations are a useful computational tool in fields such as fusion research. Small but vital portions of fusion reactors are essential to their correct operation and longevity. Using the reactive bond order (REBO) and adaptive intermolecular REBO potentials, it is possible to model carbon-based systems, such as graphite diverter plates, under simulated bombardment. The degradation of these plates due to random bombardments from plasma can eventually incur costly shut downs. To gain a better understanding of the atomic-level dynamics that occur when a graphite and amorphous carbon surface undergo energetic, serial bombardment by atoms such as hydrogen, deuterium, and tritium, these two systems were evolved with the REBO and AIREBO potentials. It was found that the AIREBO potential gave different results with regards to surface evolution, sputter yield, and steady state formation. Graphite surfaces evolved to a much different steady state when compared to amorphous carbon, which lead to varied surface structure and may also lead to differing sputtering yields.

An additional round of simulations was performed on graphite surfaces that were deeper in the direction normal to the surface. Based on the previous results, the AIREBO potential and two different bombardment energies were used, and the additional layers added allowed for greater fluences, defined by the number of impacts per unit area, to be achieved. As an additional improvement of the previous work, thermostats were set by using zones of control rather than employing the thermostat on the entire system, achieving atomic layer control of the thermostatted regions during the simulation.

After employing these changes and evolving the simulations for only slightly larger fluences than previous simulations, the formation of voids within the graphite layers, or "bubbles", was produced. Particle build-up consisting of gaseous D, D_2, and other small molecules near the penetration depth caused the formation of these bubbles. It was found for 20 eV impact energies the penetration

depth is well defined, because of the lower energy of insertion. The stopping power of the potential on these low energy insertions leads to a noticable build-up of D atoms near the penetration depth. For the 80 eV simulations, the penetration depth is broadened when compared with the 20 eV simulations. The impacts penetrate more layers with increased impact energy, with bubble formation occurring away from the average penetration depth. A comparison of retention ratios is also discussed, and found that the 80 eV simulations retained more D than the 20 eV simulations.

To attempt to avoid the issue of bubble formation, and to expand on the capabilities of the MD code, graphite surfaces were expanded in the directions perpendicular to the insertion direction, and the ability to bombard the surface with multiple atom types was implemented. Another improvement was introduced in the code to allow the variable time step algorithm to be used in conjunction with the thermostat. These systems yielded a closer model to experimental conditions, where the energy of interaction between the layers of graphite is larger than the insertion energy of the incident particles. While only smaller fluences compared to previous work have been achieved for these systems, the systems have shown promise in terms of their surface evolution and behavior.

Acknowledgements

Firstly, I would like to thank my Lord and Father for His inspiration and guidance. Without my faith, I would not have made it to this point in my life, and would certainly not make it much father than this.

Secondly, I would like to thank my advisor, Professor Steve Stuart. His unrelenting passion for science and teaching has inspired me to become a better scientist. Not just yearning to know more, but to *understand* more about the world around me. I've always been told to constantly ask questions, and with him as my advisor, the world seems slightly less dark, and a bit less scary.

To the loves of my life, Sharon, my wife, and Elyana, my daughter, I dedicate the knowledge within this thesis. They have both taught me so much about the world, and about myself, that I can no longer imagine my life without them. Without Sharon's generous support and Elyana's warm smile, the finishing of this work might not have been possible. I am forever in their debt for bringing new meaning and focus to my world. Love you lots, ladies.

And finally, to my parents, for pushing me harder than I would ever push myself, and and all my other friends and family. Each of you played a role that helped place me where I am today. For all the forgotten friends, and lost family, this work is a testament to all I've tried to understand, and a small volume to all I have been exposed to. Thank you all, it's been an incredible journey.

Financial support for work done in Chapter 3 by the DoD (47539-CH-MUR) and computational support provided by Clemson CITI group are gratefully acknowledged.

"It's not that I'm so smart, it's just that I stay with problems longer." - Albert Einstein

Table of Contents

List of Figures

Chapter 1

Introduction

Computational chemistry, relative to other fields of science, is still a new frontier. The ability to use computers to perform simple numerical calculations has been employed since the creation of the computer, but it was not until recently[1] that chemical equations and modern program design were used to simulate chemical systems. Since that time, many fields of modern computational chemistry have been invented, modified, and brought to the forefront of modern science. Quantum chemistry, for example, was brought to the forefront of the computational field by Pople[2]. Molecular dynamics (MD) is another tool that has been introduced to the computational sciences. Relying on equations of motion, MD simulations describe chemical systems through sequential updates, or calculations of forces, positions, and velocities[3]. These properties are affected by the potentials chosen, and can be used to model various systems such as plasmas[4], organic reactions[5], and others[6;7]

This focus of this work is MD simulations of carbon-based surfaces of both graphitic and amorphous nature under hydrogen bombardment. Beginning with a brief overview of MD, we continue by discussing the general theory and some key concepts such as integrators and thermostats. We then introduce the reactive bond order potential (REBO) developed by Brenner,[8] and discuss the enhanced version of the potential produced by Stuart *et al.*[9], the adaptive intermolecular REBO (AIREBO). Continuing by showcasing some applications of these reactive potentials, we then focus on our systems, graphite and a:C-D.

1.1 Overview and Review

1.1.1 Molecular Dynamics Simulations

The general premise of molecular dynamics (MD) simulations is to solve Newton's equation of motion for a system of molecules. In their simplest form, the equations of motion can be described as a series of derivatives. For any particle at an instantaneous position defined by $\mathbf{r}$,

$$\mathbf{v} = \frac{d\mathbf{r}}{dt} \tag{1.1}$$

$$\mathbf{a} = \frac{d\mathbf{v}}{dt} = \frac{d^2\mathbf{r}}{dt^2} \tag{1.2}$$

Where $\mathbf{v}$ and $\mathbf{a}$ are the instantaneous velocity and acceleration, respectively. While these equations are useful for calculating velocities and accelerations at certain points for a particle, they give no details on the motion of the particle through space. We can re-arrange these equations for a particle moving linearly with a constant acceleration, and solve for velocities and positions,

$$\mathbf{v} = \mathbf{v}_0 + \mathbf{a}t \tag{1.3}$$

$$\mathbf{r} = \mathbf{r}_0 + (\frac{\mathbf{v} + \mathbf{v}_0}{2})t \tag{1.4}$$

$$\mathbf{r} = \mathbf{r}_0 + \mathbf{v}t + \frac{\mathbf{a}t^2}{2} \tag{1.5}$$

Here, $\mathbf{r}_0$ and $\mathbf{v}_0$ are the initial positions and velocities, respectively. By using a known, constant acceleration, and known initial velocities and positions, new positions can be advanced, and velocities moved forward in time by selecting a time step t. The time step chosen can have a drastic impact on energy conservation, a key feature of MD simulations. If too large of a step is chosen, energy conservation becomes difficult to achieve within reasonable limits. This is due to the constraint of constant acceleration. When new positions and velocities are calculated, the acceleration is assumed to be unchanging. This assumption is true in the limit of very small time steps.

Conversely, a time step that is too small may conserve energy within reasonable limits, but evolution on large time scales becomes a laborious process. Because of this, a trade-off between speed and accuracy in the calculation is often a topic of debate when performing MD simulations. It should be noted that the energy is always conserved when employing the microcanonical ensemble method[10] (NVE) in which the number of moles, the volume of the system, and the total energy of the system remain constant. This corresponds to an adiabatic process in which no heat is exchanged. We can determine the force acting on each particle as a function of the all the coordinates of the system, $\mathbf{r}$.

$$F(\mathbf{r}) = -\nabla U(\mathbf{r}) = m\mathbf{a}(t) \tag{1.6}$$

Where m is the mass, and U is the change in potential energy. Another ensemble, the canonical (NVT) ensemble, is often employed in MD simulations when thermostats are required. Under NVT dynamics, the number of moles in a system, the volume, and the *temperature* are conserved. In the NVE environment, where simulations begin, isolated systems prohibit kinetic energy removal from the system[10]. Often, this may not be an issue. However, there are certain systems, such as bombardment or collisions[11–13] where projectiles are introduced, causing the overall temperature to increase. While this temperature spike may not cause problems, prolonged or sequential introduction of energetic particles will cause a large, unphysical temperature increase. In this case, a thermostat is introduced. These thermostats serve the role of energy sink, and can be implemented in a number of ways[14]

The Langevin thermostat is one that is frequently used in our simulations[15;16]. Originally proposed by Adelman and Doll[17], the thermostat implements random "kicks" in the force equation as in Equation 1.6. This is done by adjusting the velocities based on a scaling factor that can be modified (described below). The physical effect is similar to running in a crowded shopping mall; bumping into other shoppers reduces or increases your velocity, depending on where the bumps originate. In keeping with the analogy, the other shoppers in the mall are not part of the system, they interact with you only, changing your velocity, which in turn changes your kinetic energy. This then changes the temperature. The effect on molecular systems is two fold. The atoms' velocity is changed, which also changes the temperature. In equation form, for a force as a function of all the

coordinates of the system *F(**r**)*, written as:

$$F(\mathbf{r}) = m\mathbf{a}(t) = -\nabla U(\mathbf{r}) - \gamma(V(t)) + \mathbf{L}(t) \tag{1.7}$$

Here, γV is a frictional force that allows the temperature to decrease, since γ is always a positive value. $\mathbf{L}(t)$ is randomly generated noise and is a random force provided by the thermostat, with a variance that is the function of the temperature and time step. Each atom then essentially becomes coupled to its own heat bath, and follows Langevin's equations of motion. One advantage of the Langevin thermostat is its ability to dampen individual vibrational modes within a certain bond type if desired.

Without involving the Langevin thermostat, we can use Equation 1.6, to determine the force as the negative gradient of the potential, U, chosen for the simulation. These potentials, or force fields, can take various forms; some of them are discussed in the next Section 1.2 below. The forces are determined from the chosen potential, and the acclerations are calculated, while equations 1.3, 1.4, and 1.5, are used to update the positions and velocities. While using the Langevin thermostat, we instead use Equation 1.7 to determine the force.

For better energy conservation when running NVE dynamics, a different method of integration can be used, known as the velocity verlet method[18]. This method calculates velocities with the full acceleration and only half the value of the time step, updates the positions of the atoms, recalculates the acceleration based on the forces from the new positions, and finishes by updating the velocities, again with half of the specified time step value. In equation form,

$$\mathbf{V}(t + \frac{1}{2}\Delta t) = \mathbf{V}(t) + \frac{1}{2}\mathbf{a}(t)\Delta t \tag{1.8}$$

$$\mathbf{r}(t + \Delta t = \mathbf{r}(t) + \mathbf{V}(t + \frac{1}{2}\Delta t)\Delta t \tag{1.9}$$

After this step is completed, it is possible to derive $\mathbf{a}(t + \Delta t)$ from the potential by using the positions calculated in Equation 1.9. In Equation 1.8, the velocities are advanced using only half of the selected time step, thus allowing for better energy conservation for the step. Once these

two steps are performed, the velocity is again calculated with half of the time step,

$$\mathbf{v}(t + \Delta t) = \mathbf{v}(t) + \frac{1}{2}(\mathbf{a}(t) + \mathbf{a}(t + \Delta t))\Delta t \tag{1.10}$$

Equations 1.8 through 1.10 are then repeated until the maximum number of steps is completed.

1.2 Potentials (Force Fields) In MD Simulations

A key component of MD simulations is the potential, or force field, that is chosen. There are many different kinds of force fields to choose from. Some potentials use quantum mechanical adaptations to solve for the equations of motion and evolve the dynamics of the system. A subset of these potentials are known as tight-binding potentials, and can vary widely based on the atoms being studied.[19]

Pairwise potentials are popular potentials in which the total potential energy is calculated through a sum of energy contributions between pairs of atoms. The non-bonded Lennard-Jones (LJ) potential is an example of this, and is often used to calculate van der Waals forces. The standard Morse[20] and simple Coulomb potential[21] are more examples of pair potentials.

A subset of pair-wise potentials are the many-body potentials, where the full potential energy cannot be found by a simple summation of pairwise terms, as in the case when angular terms are incorporated. A classic example is the Tersoff[22] potential, where an important contribution to the energy is realized in groups of three atoms. Here, the angle between these atoms plays a key role in the total potential energy.

The reactive empirical bond order potential, developed by Brenner *et. al.*[8] is a many-body potential that utilizes some pair wise summations in its calculation of the total energy. The REBO force field contains three main components, and is given by

$$E_b = \sum_i \sum_{j>i} [V^R(r_{ij}) - b_{ij} V^A(r_{ij})], \tag{1.11}$$

where E_b is the bonding energy, V^A is an attractive pairwise term, V^R is the repulsive term, is given

by

$$V^R = w_{ij}(r_{ij})(1 + \frac{Q_{ij}}{r_{ij}})A_{ij}e^{-\alpha_{ij}r_{ij}} \tag{1.12}$$

where the parameters Q_{ij}, A_{ij}, α_{ij} depend on the types of atom being considered (carbons, hydrogens). The attractive term, V^A, has the form

$$V^A = -w_{ij}(r_{ij}) \sum_{n=1}^{3} B_{ij}^{(n)} e^{-\beta_{ij}^{(n)} r_{ij}} \tag{1.13}$$

which has parameters B_{ij} and β_{ij} based on the value of ij. In this equation and Equation 1.12, w_{ij} is a bond weighting factor that smoothly switches to zero as bonds go beyond normal bond distances.The V^R and V^A portions represent the interatomic repulsions and attractions from valence electrons, respectively. The bond-order term, (b_{ij}), is a modified from the Abell-Tersoff[23] potential, and has the form

$$b_{ij} = \frac{1}{2}\left[p_{ij}^{\sigma\pi} + p_{ji}^{\sigma\pi}\right] + \pi_{ij}^{rc} + \pi_{ij}^{dh}, \tag{1.14}$$

where $p_{ij}^{\sigma\pi}$ and $p_{ji}^{\sigma\pi}$ depend on the local coordination and bond angles of atoms i and j, π_{ji}^{rc} depends on the radical character of the i-j bond and its position in a conjugated system. The π^{dh} term is dependent on the dihedral angle for carbon-carbon bonds.[8] This model does not make the assumption of valence orbital hybridizations, and it is instead calculated explicitly by the potential as covalent bonds breaking and reforming.

While the REBO potenial (1.11) models only covalent interactions, the AIREBO potential[9] offers a significant improvement by incorporating two additional terms into the energy calculation: a long ranged adaptive Lennard-Jones (LJ) interaction, and a torsional interaction, which are written as

$$V_{ij}^{LJ} = 4\varepsilon\left[\left(\frac{\sigma_{ij}}{r_{ij}}\right)^{12} - \left(\frac{\sigma_{ij}}{r_{ij}}\right)^{6}\right] \tag{1.15}$$

$$V^{tors}(\omega) = \varepsilon\left[\frac{256}{405}\cos^{10}\frac{\omega}{2} - \frac{1}{10}\right]. \tag{1.16}$$

The LJ interaction is modified by various splines and cutoff functions[9] depending on the

chemical environment of the bond being evaluated. The constants of the torsional interaction were chosen to reproduce a threefold angular potential with a barrier height of ε when summed over the nine dihedral angles between identically substituted sp^3 carbons. For a full explanation of the terms, see Stuart *et al.*[9]

1.3 Applications of Reactive Potentials in Fusion Science

Reactive potentials describe a chemical reaction by modeling a continuous energy landscape. The process of atomic hybridization is not assumed or declared at the beginning of a reaction. As the simulation continues, atoms are analyzed based solely on their chemical environment. This makes reactive potentials useful for describing the transitions of chemical processes. Reactive potentials are useful for a variety of chemical systems, and can be applied when modeling of the reactants is required for an accurate description of the chemical process.

One application that involves reactive potentials is fusion science. While some computational models focus on the plasma contained within the fusion vessel, other models are concerned with the interactions of the plasma with various parts of the vessel.[24] Perhaps the most pressing issue within fusion science is the lifetime of the containment vessel and the parts within it. Diverter plates, often composed of graphite[11], are used to direct gases both toward and away from the plasma inside the vessel, have been the focus of intense experimental studies[11–13;25;26]. The stability of the diverter plates is often compromised via impact from random, scattered atoms and ions such as H, H^+ , D, D^+, T, and T^+[27] with a variety of energies.[28;29] These impacts can cause physical and chemical changes to the system and can lead to physical and chemical sputtering events. The resulting ejecta can interact with the plasma, which are impurities that affect the overall performance of the reactor. A consequence of this is an increased likelihood of reactor shutdown, resulting in costly cleaning measures.

To reduce this long-term expense, and to understand the chemistry involved in the processes, computational studies have been performed in conjunction with experimental work[30;31] to understand the long term effects of bombardment on both amorphous carbon and graphite.[15;16] Other properties such as the effect of vibrational state,[32;33] isotopic effects,[34–38] reflection coefficients,[39] and collision cascades[40] have also been studied computationally and experimentally. Authors such as Reinhold, Stuart, Krstic, and others[15;16;34–36;41–45] have performed bombardment

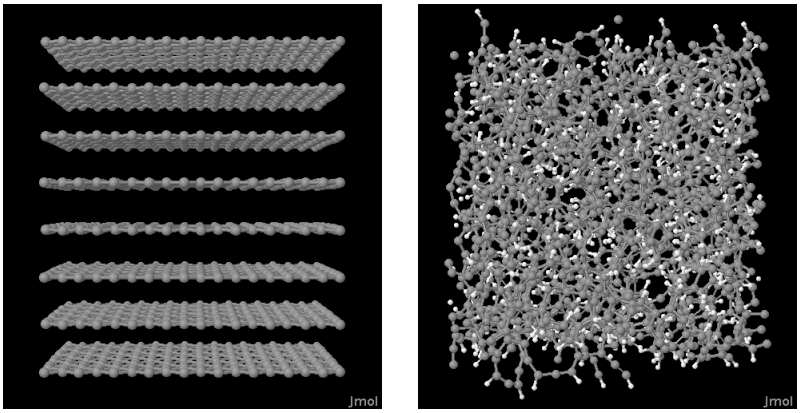

Figure 1.1: Image of a clean sheet of graphite composed of eight total layers, each with 180 atoms(left panel), and an image of a clean a:C-D surface, composed of 1440 atoms (left panel). Boundary conditions are periodic in the x and y directions, with no periodic boundaries in the z direction.

simulations of a pre-constructed amorphous carbon system to moderate fluence values of around 4.0×10^{20} D m^{-2}. They have noted the surface achieved a "steady-state" when the experimental sputtering yield remains constant relative to the particle flux.[46]

After these amorphous carbon systems have been evolved by serial bombardment in simulations, sputtering yields can be calculated and compared to experimental results.[47–49] Until recently,[15] no computational comparison of the composition of graphite and amorphous carbon systems after bombardment at high fluences has been made. Based on experimental findings,[11;12] it had been assumed that the composition of the graphite system after sequential bombardment is similar to that of amorphous carbon. However, recent evidence[15;16] has suggested that the compositions of the surfaces become substantially different, and their evolution with increasing fluence leads to two independent steady states. An image of these two surfaces is shown in Fig. 1.1, and is discussed in detail in Chapters 2 and 3.

1.4 Project Overview

Chapter 2 presents a brief summary of the modified surface for both the graphite and a:C-D systems, while Chapter 3 presents the damage sequential impacts cause on graphite and a:C-D systems. It also presents a quantitative view of the steady state surface as a basis for comparison of the two starting systems. Chapter 4 presents an extensive characterization of void phenomena

appearing in select bombardment simulations with graphite, and offers a theory of bubble formation from these simulations. Finally, Chapter 5 summarizes the main improvements, enhancements, and fixes employed for the bombardment simulations, including the addition of multiple atom types and the expansion of the graphite systems in the plane perpendicular to the plane of impact.

Chapter 2

Bombardment of Carbon Surfaces: Early Analysis

The bombardment of both graphite and deuterated amorphous carbon surfaces with 20 eV D atoms has been performed using molecular dynamics simulation. The primary purpose of these simulations was to determine whether the eventual state of the surface, once it has reached a steady state, is independent of the starting structure. It was found that while independently realized amorphous carbon structures give rise to similar impact-modified surfaces, the graphitic surface evolves towards a somewhat different structure. Including or neglecting a realistic treatment of the nonbonded interactions in the graphite bombardment does not result in large differences in the impact-modified structure, although the penetration depth was considerably less when nonbonded interactions are included.

Significant portions of this work was previously published in a peer-reviewed journal as: Stuart, S. J., Fallet, M, Krstic, P. S., and Reinhold, C.O., *J. Phys.: Conf. Series*, vol. 194. pp. 012059, 2009.

2.1 Introduction

Ion-surface collisions are relevant to a wide variety of scientific and technological applications, ranging from astrophysical systems to surface analytical methods and plasma-surface inter-

actions. In particular, impact of hydrogen, especially its heavy isotopes, on carbon-based materials is of relevance for magnetically confined hydrogen fusion plasmas, in which graphitic materials are often used as plasma-facing components, due to their advantageous thermal and mechanical properties, as well as their low atomic number. Consequently, there has been a great deal of interest in the sputtering of graphite and amorphous carbon by atomic, ionic, and molecular hydrogen isotopes, much of it at the chemical sputtering energy range of between 5 eV and ∼100 eV.[27;50;51] Previous work has included both experimental[25;27;51–55] and computational[34;35;41;42;49;53–61] approaches, using both monoenergetic beams and plasmas.

One key observation that arises from recent comparisons between simulation and experiment is the importance of surface treatment.[53–55] The sputtering takes place at a surface that has been modified by interactions with the beam or plasma, and sputtering properties are highly dependent on this modified surface structure. Thus, early simulations bombarded surfaces such as hydrogenated amorphous carbon (a-C:H), typically constructed by heating and annealing a randomly constructed surface in an attempt to mimic a beam- or plasma-modified surface.[53;56;57] More recent simulations, however, have discovered that the surface composition and morphology are very sensitive to the bombardment conditions, and that structural and sputtering properties are dramatically different for a worn-in surface than for as-constructed amorphous surfaces that have experienced no impacts.[34;41;42;58–60] The current understanding is that each particular set of beam or plasma conditions drives the surface composition towards a unique steady state composition, and that sputtering simulations must be performed on a carefully prepared steady-state surface which mimics all experimental parameters in order to reproduce experimental results. We here define a *steady state hypothesis* which assumes that the steady state depends on the bombardment conditions, but is independent of the initial state of the surface from which it evolves. In our analysis, we define the steady state to be the state of the surface at which the varying ratios hydrogen and carbon density remain constant, even while the surface is eroded with sequential bombardments. The former assumption has been verified many times: the worn-in surface structure clearly varies with different impact conditions.[34;35;42;49;59–61] However, the latter assumption — that different initial surfaces will (eventually) evolve towards similar steady state compositions under identical bombardment conditions — has been tested only for structurally similar surfaces, such as independent realizations of a-C:H. The validity of this assumption determines whether it is necessary to reproduce the exact initial surface structure in order to model a specific experiment, or whether it

is acceptable to begin with an initial surface such as a-C:H that is already similar to the expected steady state.[34;54;59] The purpose of the current work is to examine this question in some detail, by investigating the evolution of the surface towards an eventual steady state for more chemically dissimilar initial states: crystalline graphite and a-C:H.

2.2 Computational Methods

In the simulations performed here, systems of both deuterated amorphous carbon (a-C:D) and graphite were bombarded by deuterium atoms, and the resulting dynamics were studied by molecular dynamics with two different potential models.

The graphite system comprised 1440 atoms in eight layers. Periodic boundary conditions were imposed in the two Cartesian dimensions parallel to the graphite layers, with box lengths of 22.151 Å and 21.315 Å. The graphite layers were initially separated by 3.35 Å, resulting in a system size of 23.45 Å in the direction perpendicular to the graphite layers, which we label z. The system size was free to change in this direction, as periodic boundary conditions were not applied in this dimension. An a-C:D system consisting of 1750 C atoms and 750 D atoms was constructed as in previous work[41;59] by quenching a sample of molten carbon, inserting deuterium atoms to obtain a D:C ratio of 0.4, followed by high-temperature equilibration and another quench. As with the graphite system, periodic boundary conditions are imposed only in the x and y dimensions, each with length 26.506 Å. Two independent a-C:D systems were constructed with the same procedure, for use in determining the effect of small statistical differences in surface structure. The graphite and a-C:D systems were all equilibrated at 750 K using a Langevin thermostat before beginning bombardment.

All three simulations were performed with the REBO potential, which is able to treat covalent bonding interactions in hydrocarbon systems, and was originally developed for chemical vapor deposition.[62;63] The REBO potential does not include any treatment of nonbonded interactions, such as dispersion and exchange repulsion, both of which are important in order to model the graphite system accurately. Consequently, the bombardment of the graphite system was also modeled independently with the AIREBO potential, which is an extension of the REBO potential to include these nonbonded interactions.[9] Most previous simulations of sputtering of a-C:H have been performed with the computationally less expensive REBO potential, with the assumption that non-

bonded interactions are generally negligible in network solids such as a-C:H at impact energies above the sputtering threshold.[34;41;42;49;53;56;58–61] A few previous simulations have used AIREBO,[35;57] although none have examined the effect of the potential on surface modification. Thus, we bombarded four systems in total: graphite and two independent a-C:D surfaces with REBO, and graphite with AIREBO.

The bombardment was performed by introducing a D atom at least 12 Å above the surface, at a random lateral position, with a kinetic energy of 20 eV directed normal to the surface. The surface was allowed to evolve freely for 2.0 ps after the impact, after which point a Langevin thermostat with a target temperature of 750 K and a time constant of 100 fs was applied to the surface for another 2.0 ps in order to remove the deposited thermal energy. During the 2.0 ps of unconstrained dynamics, the molecular dynamics used a variable-timestep integrator.[64] Allowing the integration timestep to change during the simulation is important for sputtering simulations, as the very small timesteps that are needed for adequate energy conservation during the collision cascade would be extremely inefficient when modeling merely thermal motion. The average timestep during the early phases of the collision was ∼0.001 fs, while the timestep rose to ∼0.2 fs in the second ps after the impact. During the thermostatted portion of the dynamics, a constant timestep of 0.25 fs was used.

In order to keep the impacts from imparting any net momentum to the substrate, a portion of the system farthest from the impact interface was constrained to have a fixed position in the z dimension during the dynamics (these atoms were unconstrained in the dimensions parallel to the interface); this portion of the surface consisted of either one layer of graphite, or the lowermost 3.35 Å of atoms in the a-C:D systems. The reduction in the number of degrees of freedom in the system as a result of these constraints was properly accounted for in calculating the system temperature.

Because the REBO potential does not include any attractive interaction between graphite layers, a single atom in each graphite layer was constrained to remain at a fixed z position; without this constraint, the momentum imparted to the surface by the impact would occasionally (and unphysically) result in exfoliation of one or more graphite layers. These fixed-atom constraints were removed, one at a time, as soon as a crosslink was formed between the constrained layer and the one beneath it.

Because there were 4.0 ps of dynamics between impacts, the nominal flux at which the bombardment was performed was 3.6×10^{28} D m^{-2} s^{-1} for a-C:D and 5.3×10^{28} D m^{-2} s^{-1} for graphite. This is many orders of magnitude larger than experimental fluences, which will only reach

$\sim 10^{25}$ D m^{-2} s^{-1} even in large fusion reactors such as ITER. The effective flux is much lower, however, because the 2.0 ps thermostatting phase serves to remove the excess thermal energy that would be dissipated in the μs or ms between local impacts at experimental fluxes.

Although we are able to model the very fast collision dynamics, as well as account for the slow thermal transport in an effective way, it is important to note that there are slow kinetic effects, such as diffusion of mobile defects, that will not occur at molecular dynamics timescales, and the simulated flux does not correspond directly to any experimental flux.

Each surface was bombarded sequentially by between 700 and 1700 D impacts, reaching total fluences of up to 3.5×10^{20} m^{-2} for the graphite REBO system. Any reflected or sputtered species were removed from the simulation cell once they reached a distance of approximately 30 Å above the interface with a center-of-mass velocity directed away from the surface; this criterion was adjusted to account for swelling of the substrate, so that particles were only removed once they were no longer interacting with the substrate.

2.3 Results and Discussion

2.3.1 Variable Time Step Approach

As mentioned before in Section 2.2, variable time step integration[64] is employed during the "free" phase of the simulations. Here, we briefly present the results of a study done with the variable time step integrator, as well as giving a brief overview of the theory.

In this approach, an energy diffusion constant is defined by the simulation. This constant, D_E, can also be thought of as an energy tolerance. At each time step, the energy variance divided by the change in time is calculated. This value is then compared to D_E. In equation form,

$$D_E \equiv \frac{\sigma^2_{\Delta E}(t)}{t}\Delta t \tag{2.1}$$

If the calculated energy diffusion is greater than the tolerance (D_E), the step is discarded and recalculated with the time step multiplied by a factor of 0.5. However, if the calculated step is within the energy tolerance, the step is accepted, the time step multiplied by a factor of 1.10, and the simulation continues.

The energy diffusion constant, D_E is an intensive property of the simulation, having units

of D m^{-2} s^{-2} $atom^{-1}$. This reduces the effect of long-time energy errors when the number of atoms in a simulation changes. Figure 2.1 shows the variation of the time step during four independent impact simulations. The particle is inserted at the beginning of the simulation, and the time step used by the simulation is recorded every 1.0 fs. The time step stays constant as the particle travels through vacuum to the surface. Upon impacting the surface, the energy of the particle is partially or fully transferred to the system, and possible bond breaking and new bond formation occurs. This series of events can occur very rapidly, and is indicated by the increasingly small time steps required to conserve energy within our defined tolerance. It is during this period the time step required to maintain appropriate energy conservation can be as low as 0.0001 fs. This period of rapid energetics and dynamics persists for approximately 100 fs. After this, the time step returned to a value close to 1.0 fs, demonstrating the dynamic nature of the bombardment simulations. The limit of the time step is related to the inserted species. Heavier atoms such as D and T will allow for a higher time step due to it's larger mass, and corresponding smaller accelerations.

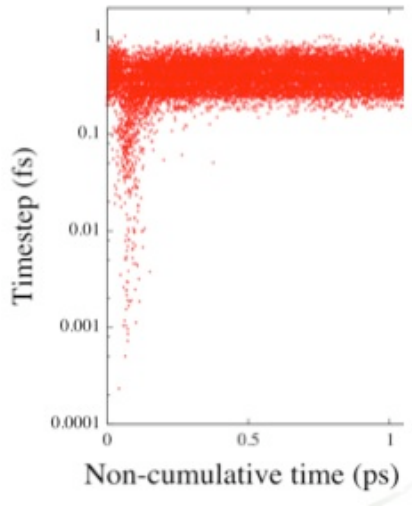

Figure 2.1: Time steps used in four non-sequential, independent D bombardments on a graphite surface for the first 1.0 ps of the simulation. Each atom was inserted at 0.0 ps, and the time step was recorded every 1.0 fs.

2.3.2 Surface Evolution and Characterization

To illustrate the evolution of the surface under bombardment, we first examine the behavior of the a-C:H surface under bombardment by 20 eV D atoms at normal incidence, with the inter-

particle interactions modeled using the REBO potential. This particular combination of surface, potential, and bombardment conditions has been studied previously,[34;35;42;54;58;59] although at a surface temperature of 300 K rather than 750 K. Analysis of the sputtering behavior of this system, in comparison with previous results, may thus yield insights into the anomalously high sputter yields at temperatures near 750 K,[50] a phenomenon that is not yet fully understood. The emphasis here, however, is on structural properties, rather than sputter yields. Figure 2.2 shows how the density of both C and D atoms evolves in this system with increasing fluence.

In the initial, as-prepared surface (at zero fluence), the carbon and hydrogen densities exhibit random fluctuations due to the finite sample size, but the average density is independent of distance from the interface. The surface composition changes, however, under bombardment. The continued bombardment by D results in decreased C density, due to erosion of C atoms that can not be replaced, and an increase in D density, due to implantation. The 20 eV D atoms modify the surface to a depth of approximately 15 Å beneath the interface, and the D:C ratio in this modified surface layer exceeds the saturation concentration of 0.4 D/C in the bulk,[65] although it does not quite reach the D/C ratios of 1.0 seen in previous work.[34;59;60]

The graphite surface was bombarded with the REBO potential in an effort to determine whether a surface with a different structure would approach the same steady state under identical bombardment conditions. This is an important comparison, since the carbon-containing plasma-facing components in many plasma experiments are initially graphitic in structure, at the nm length scales corresponding to these simulations. The present analysis thus provides a partial examination of the effect of the structure of the initial surface. A more complete study would involve additional factors such as averaging over the orientation of the graphite planes, in order to reproduce the polycrystalline structures in materials such as ATJ graphite or carbon fiber composites. The evolution of the C and D density profiles for graphite is illustrated in Figure 2.3, at fluences up to 3.54×10^{20} D m^{-2}.

The sharp peaks in the density profile indicate the layered graphite structure, at low fluences and well beneath the interface. Upon bombardment, however, the surfacemost layers lose their layered structure and become amorphous. At a fluence of $0.98\times$ 10^{20} m^{-2} (red, solid curves in Fig. 2.3), the bombardment has only affected the structure of the two graphite layers closest to the interface. The outermost layer, originally near $z = 24$ Å, has been substantially degraded, and has become largely amorphous, while the second layer has become somewhat disordered but preserves

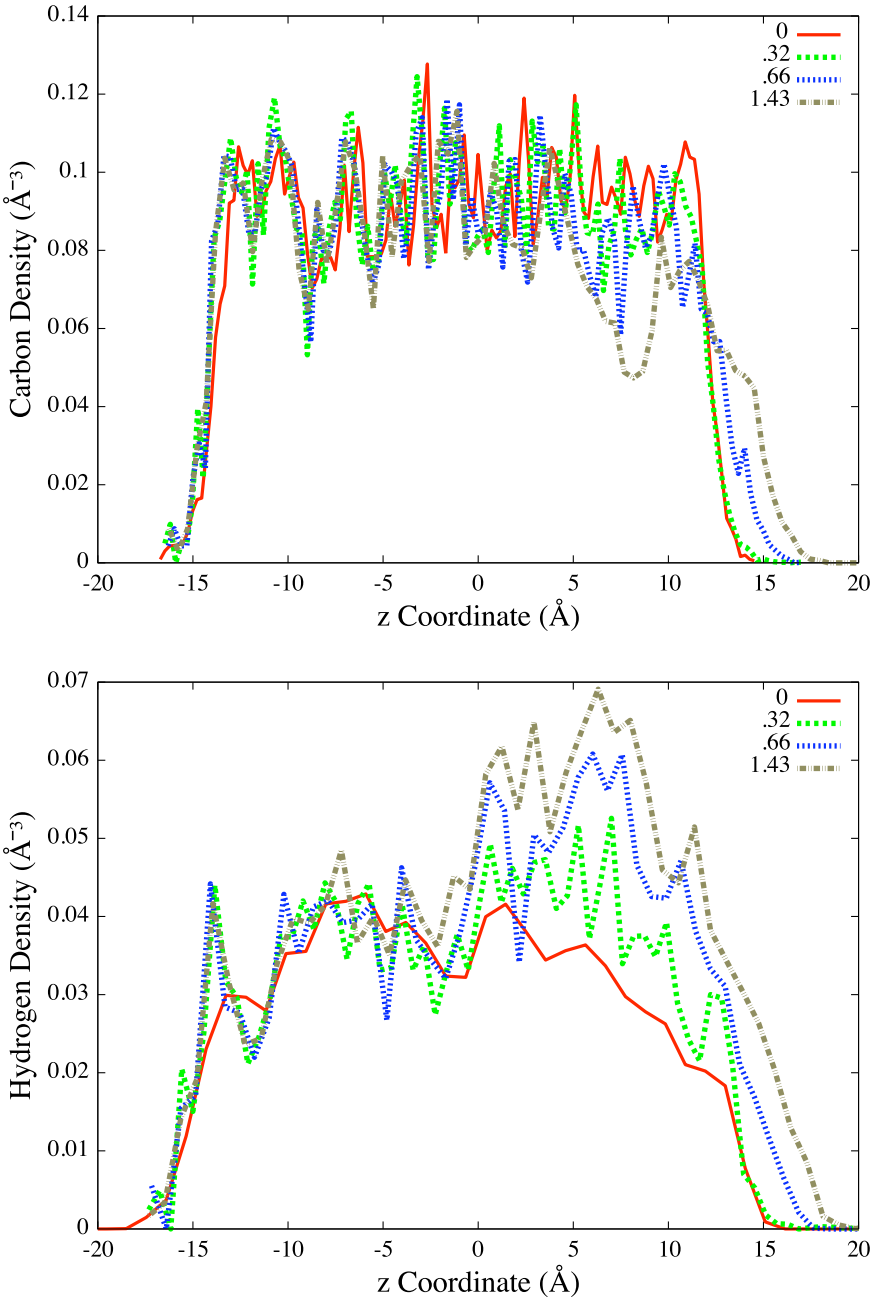

Figure 2.2: Evolution of carbon density (top panel) and hydrogen density (bottom panel) in a deuterated amorphous carbon surface under bombardment by 20 eV D atoms, simulated with the REBO potential, at fluences in units of 10^{20} D m^{-2}.

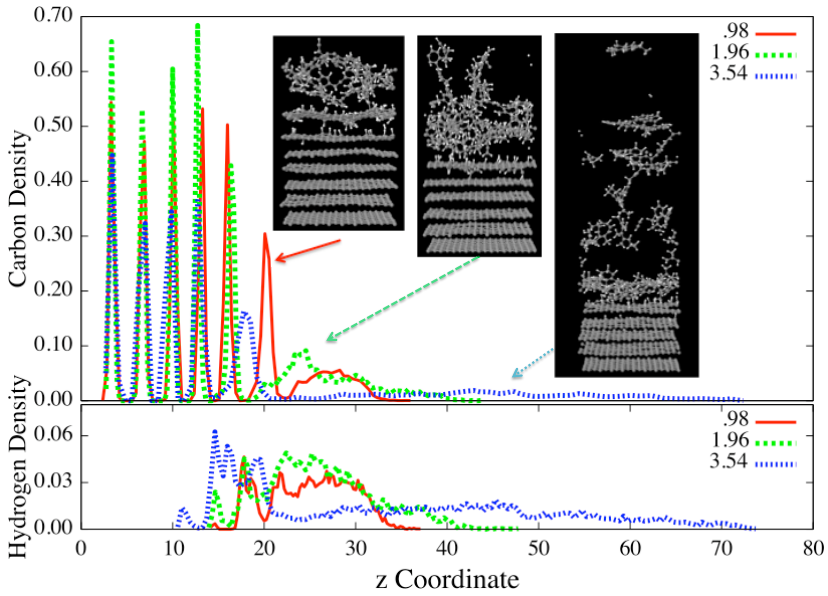

Figure 2.3: Density profiles of carbon (upper panel) and hydrogen (lower panel), in atom/Å^3, for a graphite surface under bombardment by 20 eV D atoms as simulated with the REBO potential, for fluences as indicated in the legend in units of 10^{20} D m^{-2}. The z coordinate is provided in units of Å, where the initial position of the interface at zero fluence is approximately $z = 24$ Å.

much of its planar structure. This is confirmed by the D density, which shows that D atoms are attached to the upper and lower surface of the second graphite layer (note the lack of D directly at the $z = 20$ Å position of the second layer itself), and are fully embedded throughout the now amorphous outer skin.

At higher fluences of 1.96×10^{20} m^{-2} (green, dashed curves in Fig. 2.3), this degradation has continued. The second graphite layer has become subsumed into the amorphous outer skin, which has grown to a width of approximately 20 Å, swelling some 15 Å above the initial position of the interface.

By the time the fluence has reached 3.54×10^{20} m^{-2} (blue, short dashes in Fig. 2.3, the third layer of graphite has begun to be modified, binding a substantial amount of hydrogen. The outer two layers have expanded considerably, growing to a width of approximately 50 Å, and reaching some 45 Å above the position of the initial interface. As it has swollen, the density of the modified surface has also dropped accordingly. Experimental studies have also observed the formation of low-density,

amorphous regions under bombardment, although for tungsten rather than carbon surfaces.[66] The low-density region is highly fragmented, as is visible from the inset of Figure 2.3. But when the system at a fluence of 3.54 $\times$ 10^{20} m^{-2} is simulated, post-impact, for an additional 500 ps with no thermostat and no bombardment, only 40 of the approximately 440 atoms in the low-density region desorb from the surface, illustrating that most of the fragments are properly described as part of the surface, rather than slow-moving ejecta that were trapped in place by the imposition of a thermostat. It is still possible, however, that this low-density region may be an artifact of the unrealistically small time between impacts, and that lower fluxes would allow for more complete annealing of the damaged surface; this question can not be resolved from the current simulations.

These dramatic changes, and the difference in behavior when compared to the a-C:D system, are more clearly illustrated in Fig. 2.4, where we directly show the evolution of density as a function of fluence, for both the a-C:D and graphite initial substrates. In this figure, the surface is characterized by the C and D density in the modified surface layer (not the full system). To calculate this surface-only density of C and D, the boundaries of the modified surface were taken to be those z planes at which the density began to differ substantially from the unmodified surface, for a-C:D, or at which the density drops to 10% of the peak density in the modified surface, for graphite.

The evolution of the a-C:D surface is illustrated for both of the independently constructed surfaces in Fig. 2.4 (blue [short dashed] and magenta [dotted] curves). Although these two simulations do not demonstrate identical evolution of surface properties, they are qualitatively quite similar. The difference between the two curves — on the order of 0.01 atom/Å^3 at corresponding fluences — serves as an indication of the level of statistical error that can be expected from independent realizations of different surfaces with the same average properties. We also observe from these two surface evolution trajectories that the system has not reached a true steady state, as the C and D density continue to evolve slowly at fluences of $\sim$ 1.0 $\times$ 10^{20} m^{-2}. The evolution of the surface has slowed, however, with the rate of change in the density being somewhat slower than at lower fluences. Previous simulations of a-C:D at 300 K have found that a steady state is reached at fluences of 1.0–2.0 $\times 10^{20}$ D m^{-2}, with the sputtering yield and structural properties such as surface density becoming constant to within statistical fluctuations.[35;59]

The bombardment of the graphite surface under REBO (red solid curve in Fig. 2.4), on the other hand, shows behavior that is strikingly different from that of the a-C:D surfaces. The initial graphitic state is far from a-C:D in this density space, and the surface quickly evolves towards lower

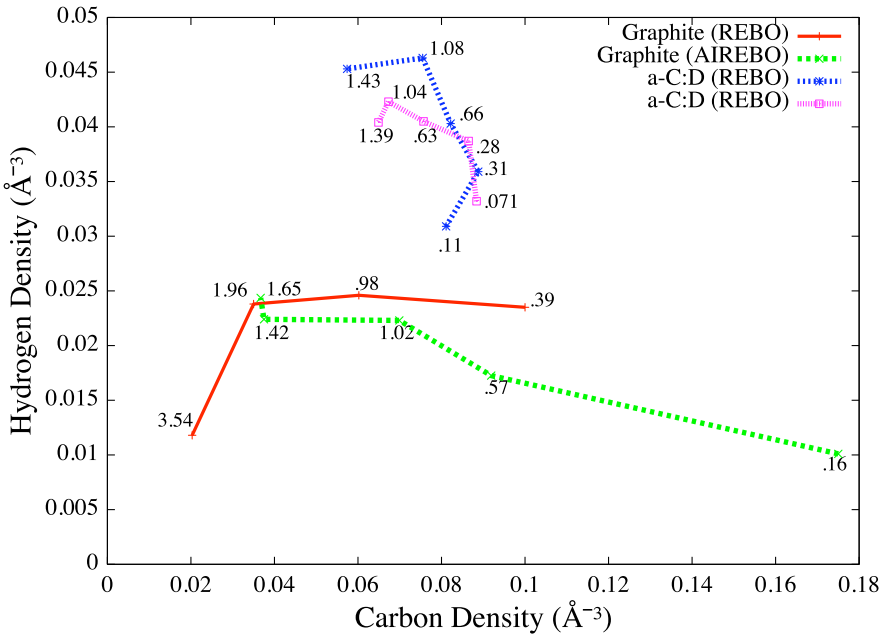

Figure 2.4: Evolution of the properties of the impact-modified surface, characterized by C and D density, as a function of fluence, under 20 eV D impacts. The surface evolution is shown for two distinct a-C:D surfaces modeled with the REBO potential, and graphite modeled with both REBO and AIREBO. Labels on each point indicate fluences, in units of 10^{20} D m^{-2}.

C density and D density, as expected. However, rather than approaching the same region in density space that the a-C:D system evolves towards, the graphite system never accumulates as much D, and eventually becomes much less populated with C atoms. And, surprisingly, the D density does not increase monotonically, but begins to decrease rapidly above fluences of 2 $\times 10^{20}$ m^{-2} as the surface swells, as was already observed in Fig. 2.3.

The graphite system was also simulated with the AIREBO potential, in order to evaluate the effect that the potential has on the surface structure. The evolution of the modified surface of this system is also shown in Fig. 2.4 (green dashed curve). Interestingly, the evolution of the AIREBO surface follows a very similar trajectory in density space to that of the REBO surface, although they are not identical. Generally, the C and D densities at a given fluence are identical to within the $\sim$0.01 atom/Å^3 tolerance that can be attributed to the statistical difference between different realizations. It would be very interesting to see whether the AIREBO potential also predicts the dramatic swelling and decrease in density exhibited with REBO at fluences above 2 $\times$ 10^{20} D m^{-2}. Unfortunately, however, the added computational expense of the AIREBO potential meant that

these higher fluences could not be reached as part of the current study.

Although the properties of the modified surface layers appear similar when characterized by just their C and D density, their structures are, in fact, different in other respects. This is illustrated in Fig. 2.5, which compares the density profiles for REBO and AIREBO bombardment of the graphite surfaces at comparable fluences of 1.6×10^{20} D m^{-2}.

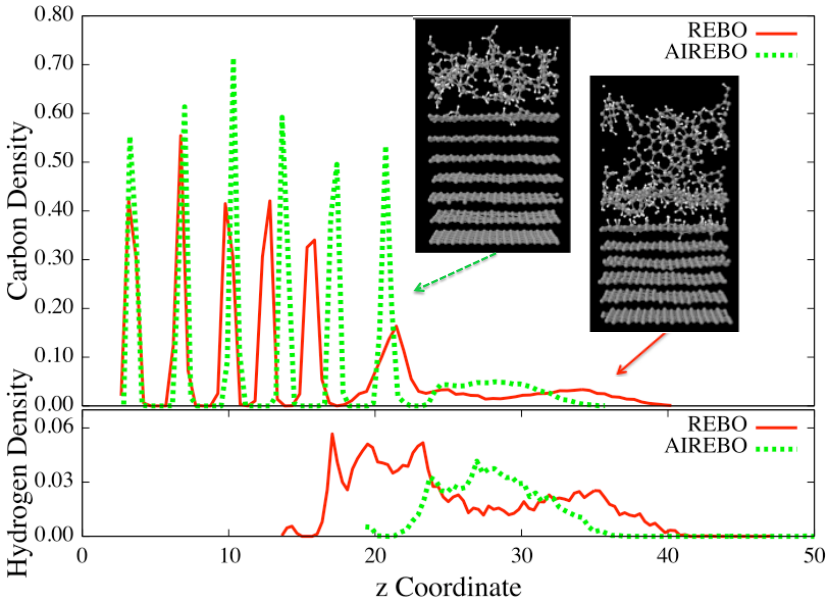

Figure 2.5: Density profile for carbon (upper panel) and deuterium (lower panel), in atom/Å^3, for a graphite surface under bombardment by 20 eV D atoms as simulated with the REBO potential (red, solid curves) and the AIREBO potential (green, dashed curves), at a fluence of 1.6×10^{20} D m^{-2}. The z coordinate is provided in units of Å, where the initial position of the interface at zero fluence is at approximately $z = 24$ Å.

Here it can be seen that, while the *density* of the modified surface layer is comparable for both potentials, the *width* of the modified surface layers is quite different. At this fluence, the REBO bombardment has amorphized the outermost layer of graphite, which has begun to crosslink with the disordered second layer, while the D atoms penetrate as deeply as the upper surface of the third graphite layer, spanning the outermost 23 Å of the surface. Under bombardment with the AIREBO potential, however, the outermost graphite layer has become largely amorphous, but the second layer is largely unmodified, and binds very few hydrogens. The hydrogens are restricted to the outermost

12 Å of the surface, within the amorphous skin. Thus, while the densities of the modified surface layers are similar, the depth of the surface modification under AIREBO is approximately half that obtained with the REBO potential. This is consistent with earlier studies, which have found that the presence of the repulsive Lennard-Jones interactions in the AIREBO potential results in larger scattering cross sections.[39]

2.4 Conclusion

In this work, we have examined the evolution of both graphite and hydrogenated amorphous carbon surfaces under bombardment by 20 eV D, using molecular dynamics simulation. These simulations reinforce results obtained in previous work, while providing new information regarding the assumption that there is a unique steady state surface composition for any given bombardment conditions.

In all cases examined, bombardment of a carbon-based surface by deuterium leads to erosion of the carbon content and accretion of deuterium. This is true even when the initial surface is consistent with amorphous carbon that has been fully saturated with hydrogen.[65] The detailed evolution of the surface composition is complex, however, and depends on the initial surface.

Independent simulations of amorphous carbon surfaces that are similar in their composition, but differ in atomic detail, result in very similar evolution of surface composition, as measured by density. The evolution of an initially graphitic surface, on the other hand, evolves towards a composition that appears to be distinct from that approached by the a-C:D, and is considerably less dense. In addition, the evolution of the initially graphitic surface is complex, with non-monotonic changes in hydrogen density. This conclusion is significant, as it appears to suggest that the "steady state" surface that is generated by bombardment, and which has been shown to have large effects on the sputtering properties of a surface, is not only a property of the bombardment conditions, but retains some dependence on the starting state of the surface, at least at the fluences examined here. Because the surfaces were still evolving at the highest fluences considered here in this experiment, we are unable to say definitively whether the two surfaces are in fact approaching different steady states. However, Chapter 3 shows that graphite and amorphous carbon do differ in their final states. This will be discussed in detail there. Extending this study to higher fluences in order to answer this question more conclusively will be important in comparing simulation to experiment. In addition,

it will be important to analyze the sputter yield on these modified surfaces, in order to determine the effect of the modified surface structure. In the meantime, this study reiterates the importance of matching the simulated bombardment conditions to the target experiment as closely as possible, not just in terms of the state of the impacting particle beam or plasma, but also in the starting substrate material.

The use of the more complete AIREBO potential, which treats nonbonded interactions that are ignored in the REBO potential, generated modifications to the graphite surface that are similar in composition to those produced with REBO, although the modification depth was less with the AIREBO potential, due to the larger cross section, and hence greater stopping power, that results from including noncovalent exchange repulsion. This will be discussed in detail in Chapter 3. The similarity in structure obtained with the two potentials provides some justification for the widespread use of the computationally less expensive REBO potential, although it remains to be examined whether the sputtering properties are similar between the two potentials.

Chapter 3

Evolution of Carbon-Based Surfaces Under Bombardment: Examining the Steady-State Surface Properties and the Effect of Potential

Chemical sputtering and erosion at carbon-based surfaces is important for many applications, such as astrophysics and plasma-surface interactions. Bombardment of deuterated amorphous carbon (a-C:D) and graphite surfaces with 20 eV D atoms has been performed using molecular dynamics simulations and two classical reactive potentials. The purpose of this work is to examine the effect of initial surface, as well as the potential energy function, on the properties of the steady state surface obtained. It has been found that while independently realized a:C-D structures evolve in a gradual process to similar impact-modified surfaces, the graphitic surface exhibits layer-by-layer, cyclical modification and evolves towards a steady state surface different from the amorphous counterpart. Longer-ranged potentials have a noticeable effect on the individual layer modification and surface structure.

This Chapter has been previously published in a peer-reviewed journal as: Fallet, M. and Stuart, S.J., *Nuc. Instr. Meth. Phys. Res. B*, vol. 269, pp 1271-1275, 2011.

3.1 Introduction

Ion-surface collisions are important in magnetically confined hydrogen fusion plasmas, astrophysical systems, and various surface analytical methods. The impact of hydrogen and its heavy isotopes on carbon-based materials is also relevant for plasma-facing components in fusion experiments, where graphitic materials are used as plasma-facing components because of their low atomic number and favorable thermal properties[36]. There has also been a great deal of interest in the sputtering of graphite and amorphous carbon by various isotopes and ions with energies varying between the 5 and 100 eV[27;50;51]. Previous work has also included both experimental[25;27;51–55;67] and computational[34;35;41;42;47;49;53–61;68] approaches.

Proper modeling of surface treatment has been shown to be an important factor when comparing experiment and simulation[15;53–55]. The beam or plasma interacts and modifies the surface, and the resulting sputtering properties are highly dependent on the surface modification. Recent simulations have shown that surface composition and morphology are also sensitive to the bombardment conditions, and worn-in surfaces present different structural and sputtering characteristics than pre-constructed surfaces[34;41;42;58–60]. These surfaces, after many sequential impacts, exhibit steady state properties that are dependent on bombardment conditions[34;35;42;49;59–61]. However, the effect of starting surface has begun to be examined only recently[15], and is discussed in detail in Chapter 2. The purpose of this work is to examine this question in some detail, by bombarding two chemically dissimilar initial surfaces, graphite and a-C:D with 20 eV deuterium (D) atoms. The effect of potential energy function will also be examined. In this Chapter, higher fluences are achieved than Chapter 2, and a much more detailed analysis of the carbon and hydrogen densities are presented in the from of individual density plots.

3.2 Computational Methods

Deuterium sputtering is performed on both a graphite surface, composed of eight layers, each with 3.35 Å separation; and on two independently realized a-C:D systems with a density of 2.0 g cm^{-3} and D:C ratio of 0.4 as used previously.[34;69] Deuterium impacts were performed with 20 eV kinetic energy directed normal to the surface (defining the z axis), and periodic boundary conditions were employed in the two Cartesian dimensions parallel to the surface. Both the graphite and a-C:D systems were equilibrated to 750 K using a Langevin thermostat before beginning bom-

bardment. Post-collision dynamics were integrated using a variable timestep integrator[64], since the timesteps required for adequate energy conservation during a collision are considerably smaller (averaging ∼0.001 fs) than those used during thermal motion(∼0.2 fs). After these 2.0 ps of unconstrained dynamics, the system was then thermostated for 2.0 ps at a temperature of 750 K using a Langevin thermostat.[15] Other details of the simulation conditions are identical to those presented in Chapter 2.

All three surfaces were modeled with the REBO potential[62;63], which does not include non-bonded interactions such as dispersion and exchange repulsion. Additionally, the graphite system and one a-C:D system were modeled with the AIREBO potential, which does include these interactions[9]. Many previous simulations have been performed with REBO[34;41;42;49;53;56;58–61], but few have used AIREBO[15;35;57]. In total, five systems are examined: graphite and two independent a-C:D surfaces with REBO, and graphite and one a:C-D surface with AIREBO.

Each surface was bombarded sequentially with between 700 and 6000 D impacts, reaching maximum fluence values of 12×10^{20} m^{-2} for the graphite REBO system. Reflected or sputtered particles were removed from the simulation cell once they crossed a plane 30 Å above the interface, with the z component of their center-of-mass velocity directed away from the surface. This plane was adjusted to account for any surface swelling to ensure that the interaction between surface and particle was zero when the ejecta are removed.

3.3 Results and Discussion

We first discuss the a-C:D surface under D bombardment with REBO to examine the surface behavior as the fluence increases. This combination of surface choice, potential, and bombardment conditions has been previously studied at 300 K[34;35;42;54;58;59]; in the current work the surface temperature is held at 750 K. Figure 3.1 shows the evolution of the carbon and deuterium density profiles at the surface under these conditions. At zero fluence, the carbon and hydrogen densities are constant (with random fluctuations because of the finite sample size), but as the fluence increases, the carbon density decreases near the surface (Figure 3.1, top panel) as the impacts erode the carbon. At comparable fluence values, the D density shows an increase, (bottom panel of Fig. 3.1), resulting from D implantation. The surface also swells to heights approximately 15 Å above the initial position of the interface, and has modified structure over a depth of nearly 30 Å.

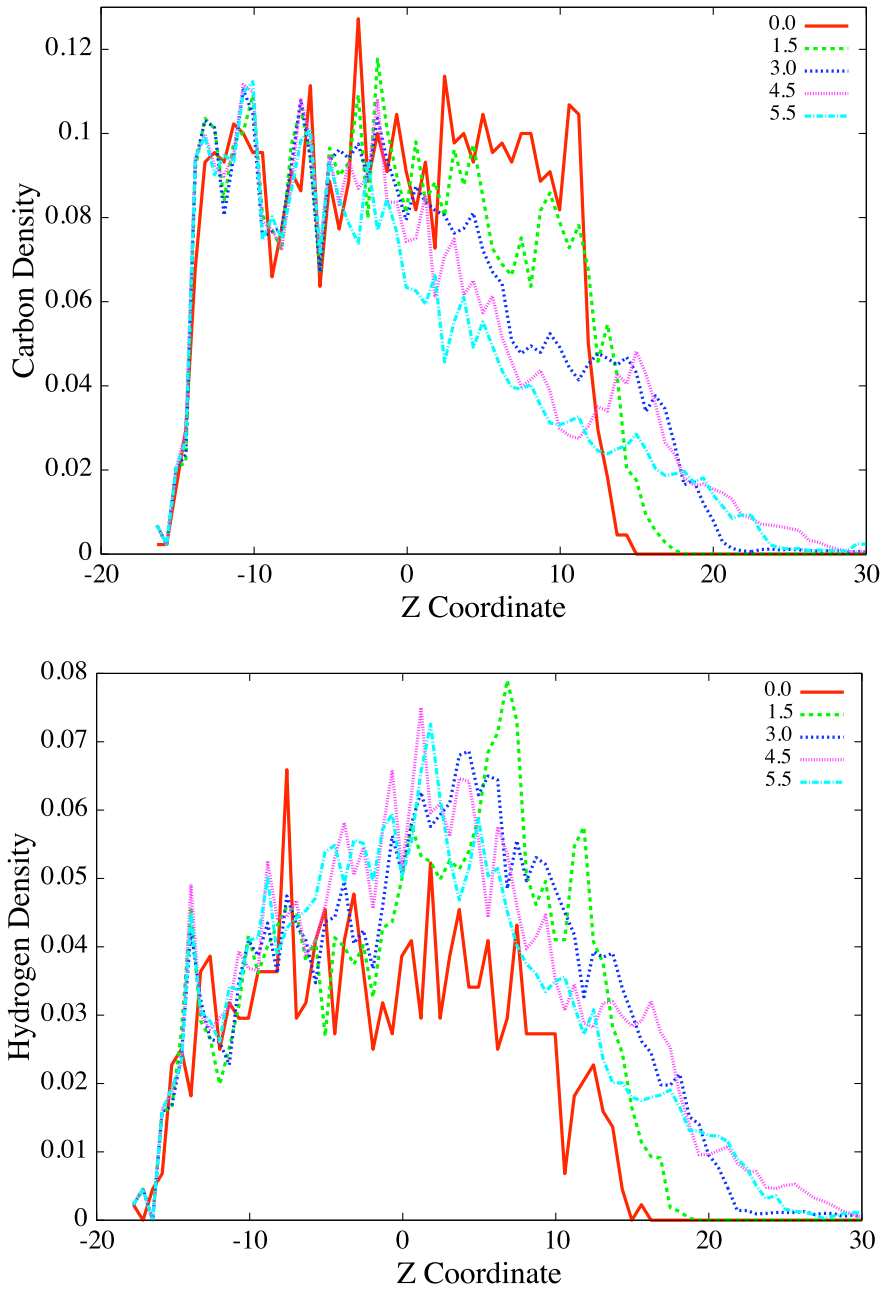

Figure 3.1: Evolution of carbon density (top panel) and hydrogen density (bottom panel) for a deuterated amorphous carbon surface under 20 eV D atom bombardment using the REBO potential (impacts from $+z$). Densities are shown at fluences listed in the legend, in units of 10^{20} D m^{-2}.

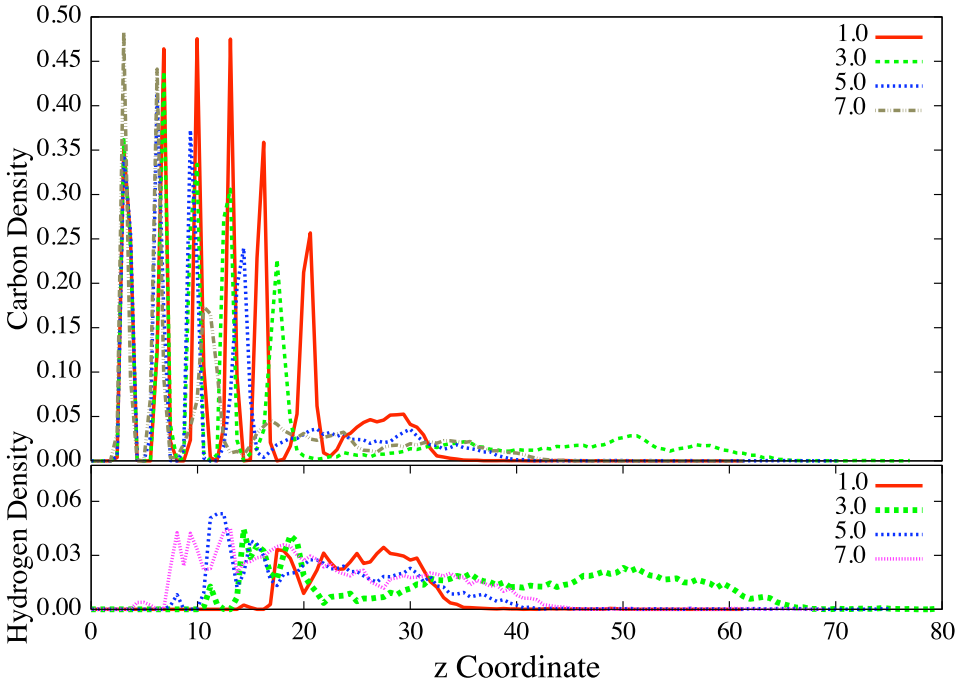

Figure 3.2: Evolution of carbon density (upper panel) and hydrogen density (lower panel) for a graphite surface under 20 eV D atom bombardment using the REBO potential (impacts from $+z$). Densities are shown at fluences listed in the legend, in units of 10^{20} D m^{-2}.

The graphite surface was also modeled with the REBO potential and identical simulation conditions to determine the effect of starting surface structure. Higher fluences are required for graphite to reach a steady state, compared to the a-C:D surface, so previous simulations have mostly begun with a-C:D. This is an important comparison, however, since many beam and plasma experiments use graphitic substrates or plasma-facing components. Figure 3.2 illustrates the evolution of the carbon and hydrogen density profiles in this simulation at fluences of up to 7.0×10^{20} D m^{-2}. The sharp peaks in C density (top panel) indicate the layered structure of the graphite surface (the rigid layer at $z = 0$ Å is not shown). Under bombardment, the width and the spacing of the uppermost graphite layers both increase, indicating that the layers swell as they become hydrogenated and more amorphous. The swelling becomes obvious when coupled with the implanted D density (bottom panel).

At a fluence of 1.00×10^{20} D m^{-2} (red, solid curve), the outermost layer has been substantially degraded and amorphized, while the second layer has kept some structure, but has been substantially hydrogenated. The D atoms have penetrated the outer two layers, and have begun to

modify the upper surface of the third carbon layer. At higher fluences of 5.00×10^{20} D m^{-2}, the outermost three layers have been fully amorphized or digested by the impacts, and the hydrogen has penetrated as deep as the upper surface of the fifth layer, at a depth of approximately 30 Å.

Under constant energy input (via impacts), the system does not equilibrate, but may reach a steady state, in which the statistical properties, such as the ratios of hydrogen and carbon density of the surface, do not change with time (although the location of the interface may progressively move downward as the surface is etched away). As with previous studies[34;41], we use the density profile as the primary indicator that the steady state has been reached. The steady state can also be characterized by sputtering yields[35;39;50], although that is not the focus of this work.

Figure 3.3 shows the evolution of the carbon and hydrogen density profiles, and can be used to identify the steady state. The surface swells initially, as deuterium atoms are implanted at 5-10 Å beneath the interface. By a fluence of $2.0–3.0 \times 10^{20}$ m^{-2}, the swelling is balanced by atom removal, as much of the carbon above the implanted hydrogen has been sputtered away. From this point on, the surface consists of a region ∼25 Å deep that is less dense and more deuterium-rich than the unmodified substrate, with the region of highest D density approximately 15 Å beneath the interface. As the fluence increases above 3.0×10^{20} m^{-2}, the surface is etched progressively deeper into the a-C:D substrate, but the composition of the outermost 30 Å remains constant (with statistical variations). Thus, we identify a fluence of 3.0×10^{20} m^{-2} as the point beyond which the steady state has been reached; at lower fluences, the surface is being worn in from the intially generated surface.

Examination of the graphite surface in Figure 3.4 using the same technique reveals different behavior. The layered structure of the graphite is clearly visible in the C density at low fluences. At a fluence of 1.0×10^{20} D m^{-2}, the outermost graphite layer has been amorphized, with heavy hydrogenation of the first two layers, and hydrogenation of the third layer just beginning. This pattern persists as the layers are etched away two at a time, with structure lost in layer n+1 and hydrogenation of the layer n+2 beginning as layer n is eroded away. The initial amorphization occurs more quickly than for a-C:D, but the steady state has an entirely different character. Indeed, rather than demonstrating a steady and continuous erosion, the graphite etching occurs in a stepwise and periodic fashion, layer by layer. Removal of each single graphite layer requires a fluence of approximately 1.7×10^{20} m^{-2} (about 800 impacts for this surface); the depth, density and composition of the surface varies depend on the phase within this removal cycle. Thus the steady state for the

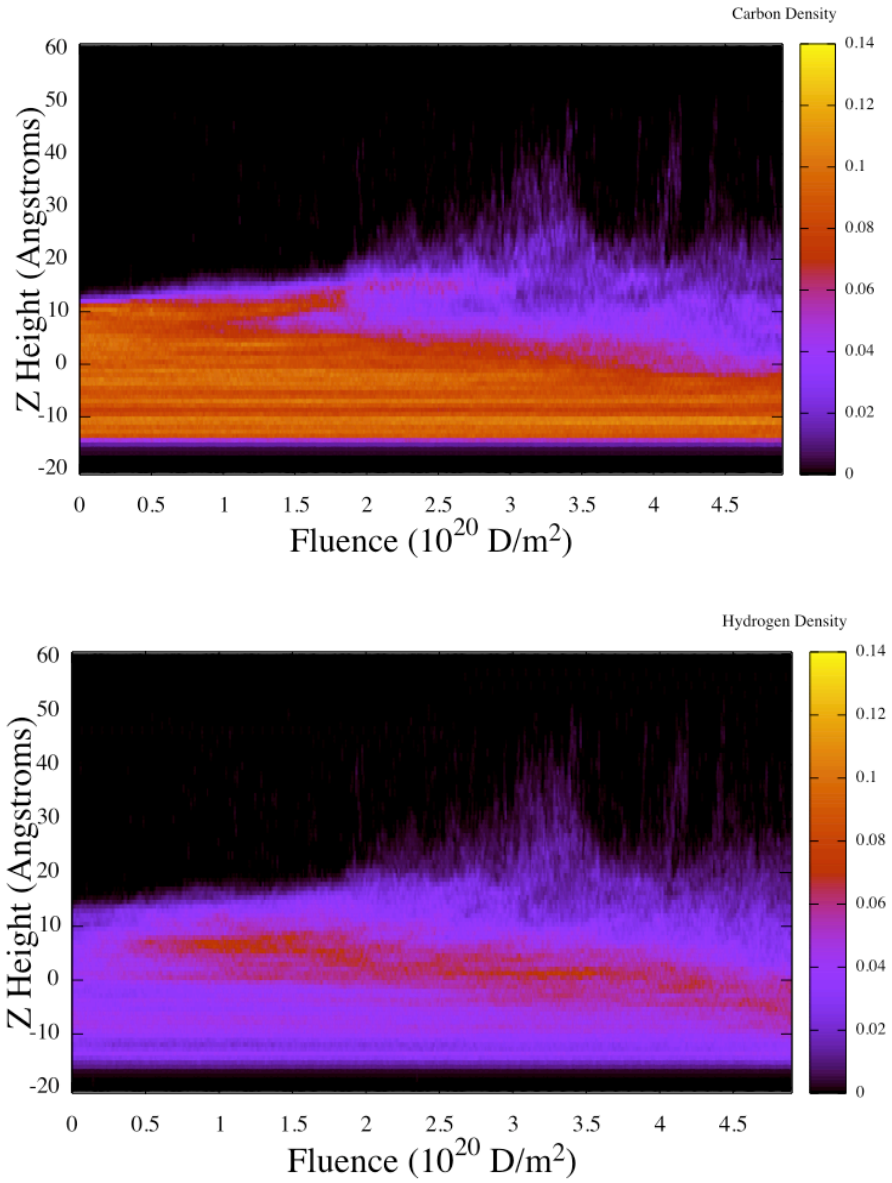

Figure 3.3: Cross-sectional density of carbon (top panel) and hydrogen (bottom panel) for a deuterated amorphous carbon surface under 20 eV D bombardment using REBO (impacts from $+z$).

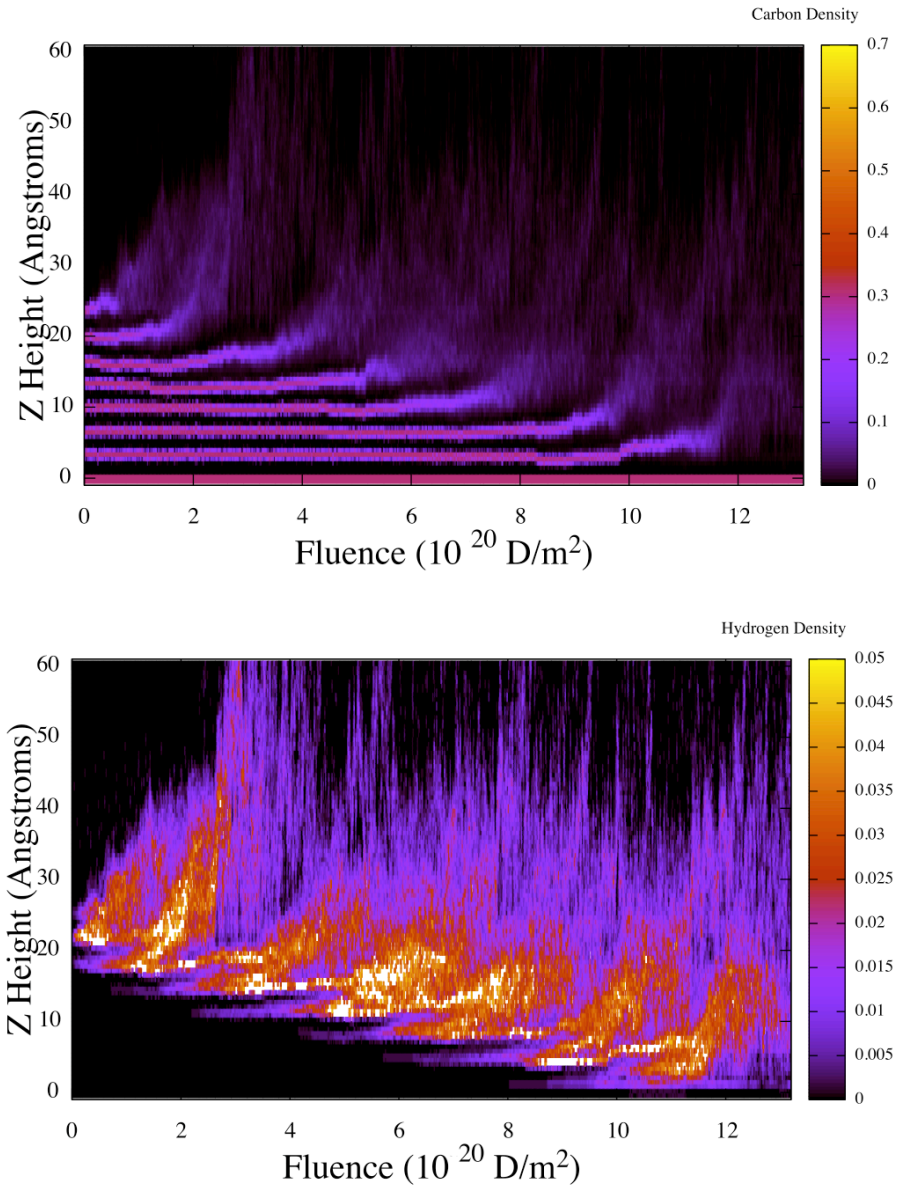

Figure 3.4: Cross-sectional density of carbon (top panel) and hydrogen (bottom panel) for a graphite surface under 20 eV D bombardment using REBO (impacts from $+z$).

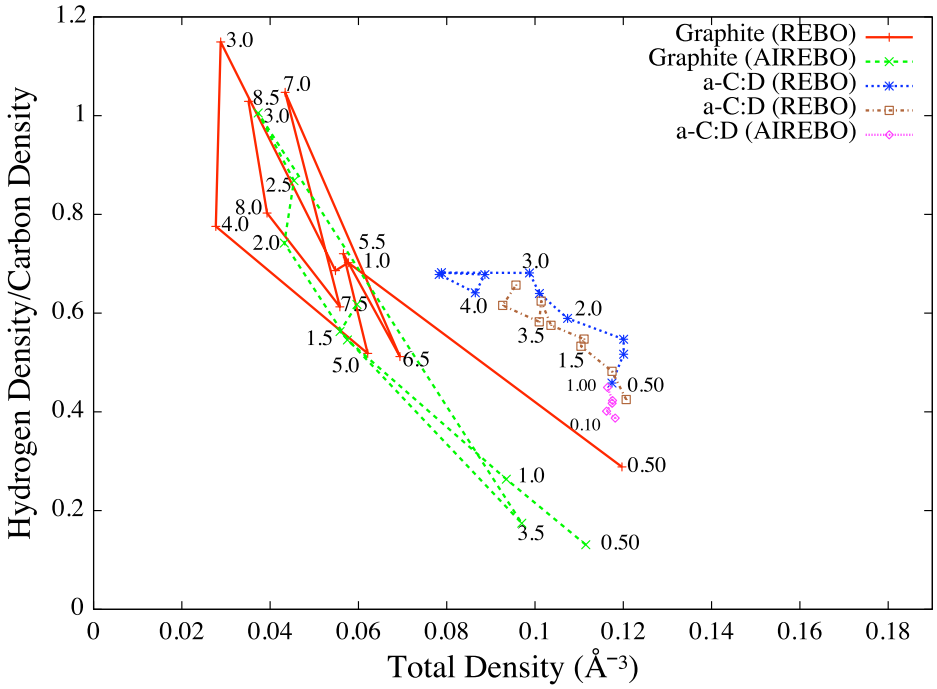

Figure 3.5: Evolution of surface, as characterized by the total density and the D/C ratio in the modified portion of the surface, for 20 eV bombardment of graphite using REBO and AIREBO (red solid and green dashed curves, respectively), two distinct a-C:D surfaces using REBO (blue and brown dashed), and a-C:D using AIREBO (pink). Labels on each point indicate fluences, in units of 10^{20} D m^{-2}.

graphite surface is best thought of as an average over a full cycle, but differs substantially from the steady state of the a-C:D system.

An additional perspective on the evolution towards the steady state in all five systems is shown in Figure 3.5. Because the primary characteristics of the modified surface are a decrease in total density and an increase in D content, we plot the time (fluence) evolution of each surface in two reduced coordinates: the total density and the D/C ratio in the modified portion of the surface. For all systems, the surface becomes less dense and more D rich as it evolves towards the steady state. The two independent realizations of a-C:D demonstrate similar behavior, and the differences serve as an indication of the level of statistical error in these reduced coordinates. At fluences beyond 3.0 $\times 10^{20}$ D m^{-2}, the systems evolve less directionally and remain in the same region of the density space, consistent with formation of the steady state. The a:C-D surface was also modeled with the AIREBO potential, generating a similar trajectory. But due to the low fluences achieved in this system, no conclusions can be made of the steady state character for this system.

The graphite and amorphous carbon systems modeled in Chapter 2 were evolved to lower fluences than in this Chapter. While the results of the steady state formation of for both systems was unclear in Chapter 2, the graphite and a-C:D systems do evolve to separate steady states. The AIREBO potential plays a critical role in the evolution of the surface, as well as the formation of the low density region above the surface. The longer range of interactions such as the torsional and Lennard Jones portions of the potential, contribute to less penetration than seen in the REBO potential, and Figure 3.5 shows a much cleaner removal of the low density region. This contrasts starkly with the REBO potential, where the low density region persists even after the removal of an entire, or $n + 2$ layers.

The graphite system modeled with the REBO potential exhibits strikingly different behavior, as suggested by Figure 3.4. The system quickly achieves lower C and higher D density than the initial clean graphitic state. However, rather than evolving toward the same steady state as the a-C:D system, the graphite system accumulates substantially more D than the a-C:D system as it swells to lower total density. Periodically, as modified graphite layers are progressively removed, the modified surface becomes thinner, denser, and less D-rich, until more impacts reverse the process and swell the layer with more implanted D. This periodic layer-by-layer erosion is indicated by the cyclical pattern traced in density space. There are several important differences from the a-C:D system: the steady state is more variable, generating a cyclical loop in configuration space, and occupies an entirely different region of configuration space than the a-C:D steady state, with lower density and (on average) higher D content.

The graphite surface was also modeled with AIREBO to probe the effect of potential on the modified surface and steady state generation. The surface evolution follows a similar trajectory in density space to the REBO surface, demonstrating a periodic, layer-by-layer modification. However, the two are not identical. The two systems achieve roughly the same deuterium content and total density when they are saturated with D. But as the layer is etched away, the AIREBO surface undergoes a more complete "cleaning" of the surface, in which approximately 15% of the deposited deuterium is removed, compared to ∼50% for the REBO surface. Figure 3.6 shows that this is because the hydrogen implantation depth with AIREBO is much shallower, leading to a thinner modified surface (cf. Fig. 3.4). Rather than penetrating the outermost two layers as with REBO, the 20 eV D atoms penetrate only one layer of C when modeled with AIREBO, and hydrogenate only the subsurface layer. The width of the D-enriched layer, while cyclic, never exceeds ∼20 Å

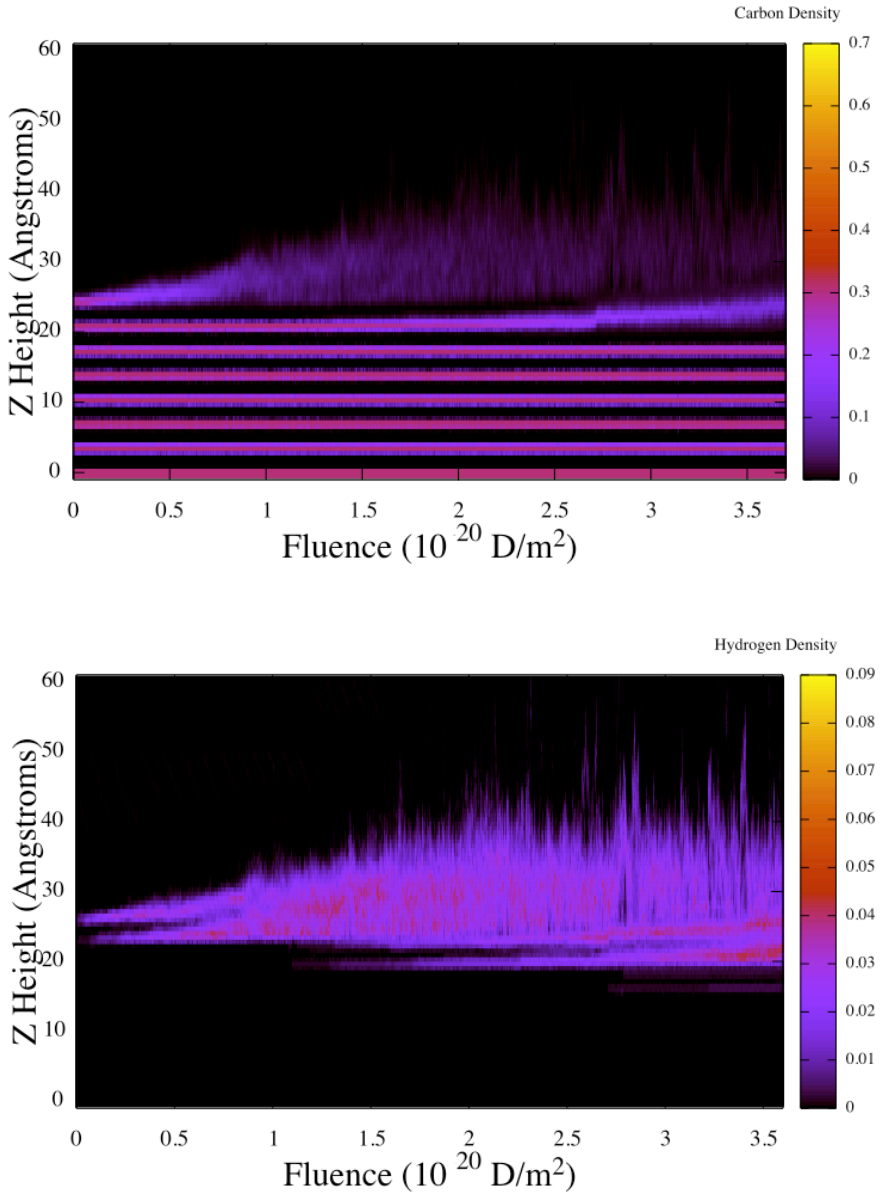

Figure 3.6: Cross-sectional density of carbon (top panel) and hydrogen (bottom panel) for a graphite surface under 20 eV D bombardment using AIREBO (impacts from $+z$).

when modeled with AIREBO, while it can be as deep as ∼40 Å when modeled with REBO. Thus when the surface layer is periodically eroded away, the substrate that remains contains substantially less hydrogen.

We speculate that the long-ranged, repulsive interactions of the AIREBO potential are significant during the collision cascade. As shown by Reinhold *et. al.*,[35], the Lennard-Jones interactions in AIREBO contribute significantly to the potential experienced by an impacting particle. For an impacting particle of the same energy, the AIREBO potential could alter its final trajectory as the incident particle begins interactions with the surface. During the equilibrium period, these same interactions may also be preventing the broadening of the low density amorphous region, contributing to formations of products that may not have interacted at all with the short ranged REBO potential

In addition, the rate of erosion is also considerably lower with AIREBO. As can be observed by comparing Figs. 3.4 and 3.6, the fluence required to etch away a layer of graphite with AIREBO is 2–2.5 $\times 10^{20}$ D m^{-2}, longer than the 1.7 $\times 10^{20}$ D m^{-2} required for REBO graphite. This lower penetration depth observed with the AIREBO potential is consistent with the higher scattering cross sections observed previously[39], and results from the repulsive non-bonded exchange repulsion (i.e. Lennard-Jones) interactions in the AIREBO potential that are absent in the REBO potential. These changes also have a measurable effect on sputter yield, although we do not present detailed sputter yield measurements here.

3.4 Conclusions

The evolution of two different carbon-based surfaces under 20 eV D bombardment has been studied with molecular dynamics simulations using two different potential energy functions. In all cases, the system evolves away from the as-generated surface towards a steady state with lower total density and higher D content. These results are generally consistent with a number of previous simulations and experiments[15;41;59;65].

For hydrogenated amorphous carbon, the steady state is reached after fluences of approximately 3.0 $\times 10^{20}$ D m^{-2}. This is consistent with a number of previous simulations, most of which have used REBO and a-C:D as the initial state.[34;35;41;42;49;53;56;58–61]

Graphite, on the other hand, evolves differently, with a cyclical, layer-by-layer surface mod-

ification, and a steady state with structural properties different than those for a-C:D, even when the properties are averaged over the cyclical trajectory in configuration space. This is an important observation, as it suggests that the steady state, and sputter yields, may depend sensitively on the choice of starting surface, at least at the fluences and temperature considered here. This is consistent with experimental studies, which have found different sputter yields for different forms of graphite[26], and it suggests that simulation studies should be careful to match their surface to the experimental results against which they compare.

The choice of potential is also seen to have a large impact on the evolution of the modified surface. The exchange repulsion interactions included in the AIREBO potential result in a larger scattering cross-section and greater stopping power than simulations performed with REBO. These, in turn, alter the character of the steady state surface generated, resulting in a shallower modified surface, less hydrogenation, and reduced sputter yields. Although the additional terms in the AIREBO potential make it more expensive to evaluate, it may be important for accurate comparison with experiment.

Some areas of improvement are needed to continue the simulations and provide a better model for experimental comparison. The use of the thermostat on the entire system, not the surface itself, is discussed in Chapter 4, and a proposed alternative thermostat protocol is presented. In addition, to achieve even larger fluences, the systems can be expanded in the z direction. Continuing the sequential bombardments in this fashion permits further study of the surface evolution as more atoms are inserted.

Chapter 4

Bubble Formation in Graphite Systems Under Deuterium Bombardment

Simulated serial bombardment of graphite systems using energetic deuterium atoms can cause void, or "bubble" formations between the graphite layers, resulting in delamination of one or more graphite layers from the surface. Two bombardment energies, 20 eV and 80 eV, are examined, and features of the bombardment such as penetration depth and retention ratio are observed. It was found that low-energy impacts provide a well defined penetration depth and generate a bubble near this depth, but have a retention ratio only near 20 %. Higher energy impacts, however, have a larger retention ratio, near 43 %, but a broadened penetration depth, leading to bubble formation that may not occur near the average penetration depth. A simple model based on the ideal gas law can be used to determine when the gaseous molecules inside the bubble overcomes the cohesive force between the layers of graphite and remove the top layers of graphite, causing a delamination event.

4.1 Introduction

In this work, serial bombardment of deuterium (D) ions were performed on two graphite surfaces with two incident energies, 20 eV and 80 eV. The collisions between the atoms and the

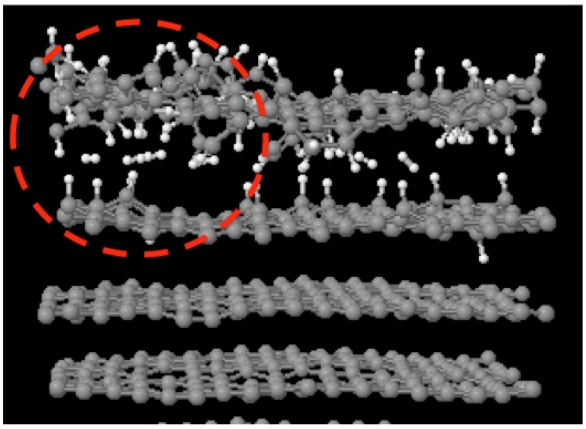

Figure 4.1: Formation of a separation of two graphite layers caused by the build-up of gaseous molecules between the layers. This build-up is a result of energetic particles impacting the surface, causing damage.

graphite surfaces caused bond formation and bond cleavage. A result of this behavior is the formation of small molecules being liberated in the spaces between the graphite layers. These gaseous particles exhibit a force on the graphite, and can separate the layers father than 3.35 Å, the average distance between graphene sheets in graphite. This separation between the graphite layers is defined as a "bubble," and Figure 4.1 provides a graphical depiction of the bubble formation. Through further sequential insertions and subsequent impacts on the surface, the number of gaseous molecules within the bubble fluctuates slightly depending on the molecule formed, but increases. This increases the force between the layers as a result of the increase in pressure due to expansion of the bubble. Once the pressure within the bubble has overcome the cohesive force between the layers of graphite, one or more of the layers is expelled from the system, depending on the position of the bubble formation. This delamination event results in the deletion of a large number of carbon and deuterium atoms from the simulation.

Bubble formation of graphite is a rarely observed phenomenon. Most often, bubble formation is seen in tungsten[70–72]. In fusion reactors such as ITER, the surface evolution and degradation of both tungsten and graphite is important to understand. Since many of the plasma facing components of the reactor are subjected to extreme conditions, the degradation of these surface may contaminate the plasma and lead to expensive repair. For graphite, many comuptational[15;16;34;35;41;42;47;49;58? ;59], and experimental[25;27;51–55] studies have been performed to analyze properties such as sputtering yield, formation of gaseous products like CH_4, the effect of

temperature, and others.

However, bubble formation within graphite surfaces were not commonly observed in the previous simulations performed in Chapters 2 and 3. In the rapidly changing experimental conditions that occur in fusion reactors such as ITER, it is likely that bubble formations cannot be detected using the standard detection methods. Bubble formation in graphite and graphene under different experimental conditions, however, has been observed. Void formation occurs when graphene is placed on an SiO_2/Si substrate and irradiated by protons,[73] These voids have even been used in conjunction with Raman spectroscopy to study the strain induced by bubble formation.[74] Thick-walled graphite bubbles have also formed in the presence of molten metals and can be characterized with techniques such as AFM, SEM, and Raman spectroscopy.[75] The formation of graphite bubbles under extreme conditions without delamination from bulk is a testament to graphite's robustness as an experimental material. However, no computational studies of bubble formation in graphite as a result of energetic bombardment by small atoms have been performed.

In this work we present two surfaces that have undergone serial bombardment by small atoms at two different incident energies. Characteristics of the surface such as penetration depth and retention ratio are presented to examine the formation of bubbles, as well as an analysis of the delamination process. Finally, we present a predictive model of graphite layer delamination using the ideal gas law and pressure imposed by the trapped gas molecules.

4.2 Computational Methods

In the simulations performed, graphite systems were bombarded by D atoms, and the resulting dynamics were studied by molecular dynamics with the AIREBO potential[9]. The graphite system comprised 2880 atoms in sixteen layers. Periodic boundary conditions were imposed in the two Cartesian dimensions parallel to the graphite layers, with box lengths of 22.15 Å and 21.31 Å. The graphite layers were initially separated by 3.35 Å, resulting in a system size of 53.6 Å in the direction perpendicular to the graphite layers, which we label z. The system size was free to change in this direction, as periodic boundary conditions were not applied in this dimension. The graphite system was equilibrated at 900 K using a Langevin thermostat before beginning bombardment. The goal of differing the temperature instead of 750 K as in Chapters 2 and 3 was to observe any difference in sputter yeilds of the graphite surface as a function of temperature. However, the emphasis

here is on bubble formation and delamination of the graphite layers rather than sputter yields

Bombardment of the graphite system was modeled with the AIREBO potential, which is an extension of the REBO potential to include several non-bonded interactions. For a full explanation of the AIREBO and REBO potentials, see Stuart *et. al.*[9] and Section 1.2. Previously studied simulations been performed with an amorphous carbon (a:C-H) system using the computationally less expensive REBO potential, with the assumption that nonbonded interactions are generally negligible in network solids such as a-C:H at impact energies above the sputtering threshold.[34;41;42;49;53;56;58–61] A few previous simulations have used AIREBO,[15;16;35;57]. and recent work discussed in Chapters 2 and 3 in this thesis has shown the importance of starting system and potential in the accuracy of the simulations when compared to experiment.

The bombardment was performed by introducing a D atom at least 15 Å above the surface, at a random lateral position, with a kinetic energy of 20 eV or 80 eV directed normal to the surface. The surface was allowed to evolve freely for 2.0 ps after the impact, after which point a new thermostatting method involving Langevin thermostat was implemented with a target temperature of 900 K and a time constant of 100 fs was applied to the surface for another 2.0 ps in order to remove the deposited thermal energy. During the 2.0 ps of unconstrained dynamics, the molecular dynamics used a variable-timestep integrator.[64] Details of the new method for Langevin thermostat implementation are described below.

Previously, the low-density amorphous region noted by Fallet *et. al.*[16] and in Chapters 2 and 3 generated by repeated impacts in graphite and a:C-H systems produces large molecules that move away from the surface. These large molecules are produced when an impact severs the last bond between the damaged graphite layer and the rest of the surface. When the thermostat is enabled over the entire system after 2.0 ps of NVE dynamics, these molecules have their velocity adjusted according to Equation 1.7, even while they are no longer part of the graphite surface. This adjustment often results in a downward scaling of the velocities to account for the temperature increase due to an insertion, and the large molecules will move slower than during an experiment, which mean lead to the formation of a low density, amorphous region above the surface. This low density region can then interfere with subsequent impacts and may produce results that are in disagreement with experiment.

While the mathematical implementation of the thermostat has not changed (see Section 1.1, the Langevin thermostat is now employed only in specified regions of the simulated system to

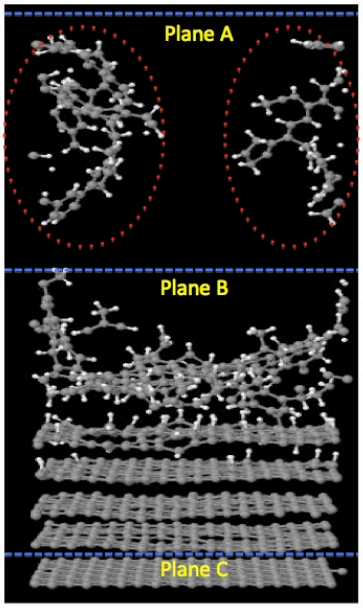

Figure 4.2: Schematic of a damaged graphite system due to bombardment with three planes (blue lines) defining zones of control, indicating regions where the thermostat is turned on or off. Large, low density amorphous material (red, dashed ovals) is being not being thermostat by the system. The top of the figure is $+z$.

thermostat smaller portions, while other areas of the entire system are not thermostated. Figure 4.2 shows the planes that define the zones used for the thermostat.

The first zone, defined as between the dashed blue line labeled plane A in Figure 4.2 and plane B, is evolved with NVE dynamics for the duration of the simuatlion. The second plane, defined as between plane B and plane C, is evolved with NVE dynamics for 2.0 ps, and the Langevin thermostat at 900 K for another 2.0 ps. Between plane C and the bottom of Figure 4.2, the atoms are kept rigid in the z direction, while evolved with NVT dynamics in the x and y directions. This was done to keep the impacts from imparting any net momentum to the substrate. This portion of the surface consisted of one layer of graphite. The reduction in the number of degrees of freedom in the system as a result of these constraints was properly accounted for in calculating the system temperature.

At any point in the simulation, these planes can be moved up and down in the z direction. The interface between the first layer of the graphite surface and the vacuum is defined by the carbon density of the graphite layer. When the accumulated damage of the graphite layer has reduced the density peak to 10% of its original density, the zone is moved further downward along the z direction,

allowing larger, slower moving particles to escape the velocity adjustments of the thermostat. The other zones are either left with NVE dynamics (between planes A and B), or the x and y positions are held constant during the duration of the simulation (between plane C and the bottom of Figure 4.2.

Allowing the integration time step to change during the simulation is important for sputtering simulations, as the very small time steps that are needed for adequate energy conservation during the collision cascade would be extremely inefficient when modeling merely thermal motion. The average timestep during the early phases of the collision was $\sim$0.001 fs, while the timestep rose to $\sim$0.2 fs in the second ps after the impact. While the thermostat is turned on, a constant timestep of 0.25 fs was used.

In order to keep the impacts from imparting any net momentum to the substrate, a portion of the system farthest from the impact interface was constrained to have a fixed position in the z dimension during the dynamics (these atoms were unconstrained in the dimensions parallel to the interface); this portion of the surface consisted of one layer of graphite. The reduction in the number of degrees of freedom in the system as a result of these constraints was properly accounted for in calculating the system temperature.

Because there were 4.0 ps of dynamics between impacts, the nominal flux at which the bombardment was performed was 5.3×10^{28} D m^{-2} s^{-1} for graphite. This is many orders of magnitude larger than experimental fluences, which will only reach $\sim 10^{25}$ D m^{-2} s^{-1} even in large fusion reactors such as ITER. The effective flux is much lower, however, because the 2.0 ps thermostatting phase serves to remove the excess thermal energy that would be dissipated in the μs or ms between local impacts at experimental fluxes.

Each surface was bombarded sequentially by between 360 and 1000 D impacts, reaching total fluences of up to 3.5×10^{20} m^{-2} for the graphite REBO system. Any reflected or sputtered species were removed from the simulation cell once they reached a distance approximately 30 Å above the interface with a center-of-mass velocity directed away from the surface; this criterion was adjusted to account for swelling of the substrate, so that particles were only removed once they were no longer interacting with the substrate.

4.3 Results and Discussion

4.3.1 Surface Analysis

A graphite system was bombarded with a D atoms with 20 eV impact energy using the AIREBO potential, and the results were examined. Initially, the carbon density of the graphite layers does not decay rapidly since the low energy of the inserted atoms do little damage to the graphite system. Figure 4.3 shows the carbon density as a function of Z distance for the graphite structure at various fluences. Figure 4.3 shows that the carbon density of the graphite layer decays as the impacts proceed, and a 25% decrease in carbon density occurs when the fluence reaches 0.35 $\times 10^{20}$ D m^{-2} (green line) as D atoms accumulate damage to the graphite layer (see Figure 4.4). The sequential impacts cause further damage to the graphite layer at a fluence of 0.49 $\times$ 10^{20} D m^{-2} (blue line).

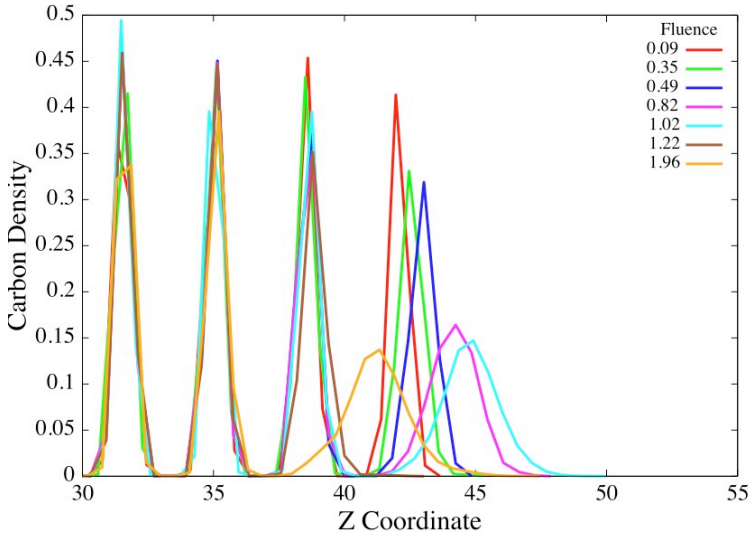

Figure 4.3: Carbon density versus z coordinate for a graphite system under bombardment by D. The impact energy of the inserted particles is 20 eV, and the units given for the fluence are 10^{20} D m^{-2}. In this figure, impacts are coming from the right, toward -z.

As the damage beings to accumulate on the first layer, a separation in seen at this fluence between the first layer and the second layer that is greater than 3.35 Å. Accumulation of D density is also seen at approximately 42.0 Å, according to Figure 4.4. It is at a fluence of 0.49 $\times$ 10^{20} D m^{-2} that bubble formation begins, when a mixture of D, D_2, and other small molecules form. At a fluence of 0.82 $\times$ 10^{20} D m^{-2} (pink line), the carbon density of the first graphite layer has degraded

to approximately 50% of its original density, based on the undamaged layers below. Also, the hydrogen density has increase substantially near 41.0 Å, indicating possible formation of gaseous D or D_2. By the time the system has reached a fluence of 1.02 $\times 10^{20}$ D m^{-2}, the delamination of the first graphite layer has occurred, ejecting the layer. The fluence of 1.22 $\times$ 10^{20} D m^{-2} in Figure 4.3 shows the delamination of the graphite layer. When the system has reached a fluence of 1.96 $\times 10^{20}$ D m^{-2}, the carbon density peak has broadened significantly and swelled, which may indicate the formation of a second bubble. Figure 4.4 shows a significant increase in hydrogen density at the second graphite layer, near 39.0 Å, which is part of a broad peak that spans from 35.0 Å to 45 Å.

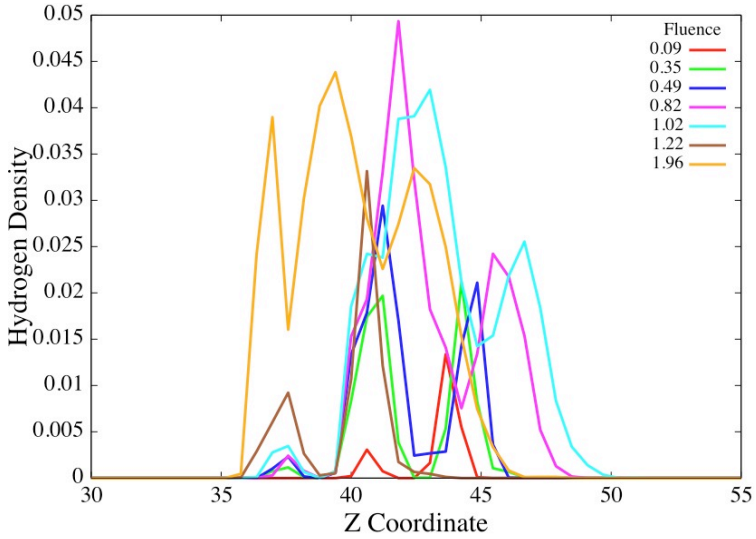

Figure 4.4: Hydrogen density versus z coordinate for a graphite system under bombardment by D. The impact energy of the inserted particles is 20 eV, and the units given for the fluence are 10^{20} D m^{-2}. Impacts are coming from the right, toward -z.

Once an atom is inserted, one of three possible scenarios can occur. If the impact is not reflected off the surface, it is then either absorbed or adsorbed onto the surface. Since only a portion of the impacted particles stay onto the surface, it is possible to analyze their position after the impact. However, an impacting particle that is not reflected off of the surface will continue to interact with other impacting particles and carbon atoms in the graphite surface for the duration of the simulation, which can last beyond 10.0 ns. The impacting particle was analyzed 5.0 ps after it was inserted into the system to determine where the D atom had embedded itself within the graphite system, but before the atom could move away from the impact area. Figure 4.5 describes the results

of the analysis.

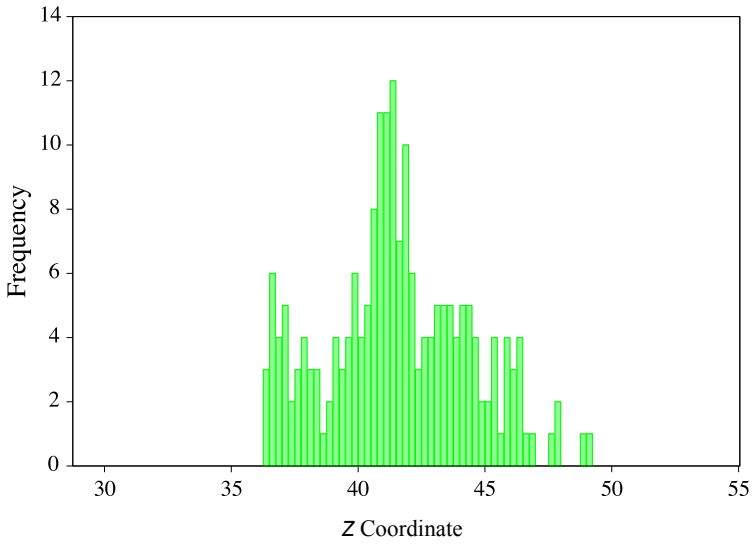

Figure 4.5: The frequency of an inserted D atom in a graphite system 5.0 ps after impact versus the Z coordinate. Each unit of frequency counts for one impact, with a total of 365 impacts inserted into the system from time $t = 0$. The energy of the impacting particles is 20 eV.

As can be seen from the Figure 4.5, a large number of D impacts come to rest around 42 Å. This corresponds to the first layer of the graphite surface (Figure 4.3). Impacts above this point are the result of the degradation of the graphite layers to form the low density, amorphous region described in Chapters 2 and 3. As the graphite layers degrade, the low-density amorphous region above the area where the bubble is formed (toward the insertion point) expands. Subsequent bombardments expand the surface further, until the bubble becomes large enough to remove the layer from the system. Once the delamination occurs, the graphite layer travels above the removal plane and is removed from the system.

We can estimate two properties in the bombardment simulations which may lead to increased bubble formation. Firstly, the penetration depth can be estimated by comparing the hydrogen density of Figure 4.4 to the carbon density of Figure 4.3. At the earliest fluence of 0.09×10^{20} D m^{-2}, the hydrogen density is visible at a distance of 40.5 Å, while the first layer of graphite has a peak density at 42.0 Å. The estimated penetration depth of the 20 eV impacts is roughly 1.5 Å, at the earliest fluence. However, after a fluence of 0.35×10^{20} D m^{-2} is reached, D density is observed between the second and third graphite layers, at 37.00 Å. This suggests the penetration depth changes as the fluence also changes, and increases to 5.00 Å after damage from the D impacts has

accumulated on the first layer. The second property to be measured is retention ratio, defined as the number of particles retained by the surface divided by the total number inserted into the system. For the 20 eV system, the retention ratio is 20%, meaning only one in five inserted D atoms. While Figures 4.3, 4.4, and 4.5 give us insight into the penetration depth and retention ratio of the 20 eV impacts, it becomes difficult to gain insight into the delamination event that follows the build-up of gaseous molecules within the bubble. With this information, a clearer picture of the bubble formation can be obtained.

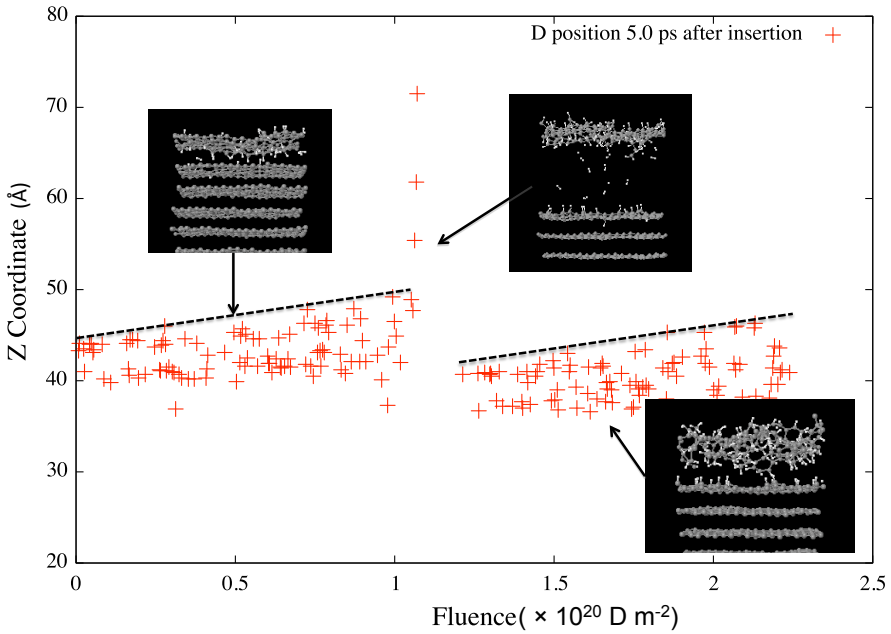

Figure 4.6: Time evolution of a graphite system under 20 eV D bombardment as a function of the z coordinate.. The insets are pictures of the system at various times. The line (black, dashed lines) is the equation used to generate Figure 4.7.

The position of the D atom is plotted 5.0 ps from the time of insertion versus time, and Figure 4.6 shows the result. The most obvious feature of Figure 4.6 is clarity of the impact placment 5.0 ps after insertion when compared to Figure 4.4. At a fluence of 0.25 $\times$ 10^{20} D m^{-2}, the impacts modify the first two layers exclusively. As the system becomes more modified, the amorphous region begins to manifest itself as the graphite layer accumulates damage. The first inset shows the modification above and below the first layer. At a fluence of 0.50 $\times$ 10^{20} D m^{-2} ps of simulation time, we begin to see the distinction between the top and bottom portion of the first layer become less pronounced, with visible hydrogen particles accumulating below the first layer as its structure

becomes less graphitic in nature. D atoms begin to appear between the layers, and the first graphite layer swells upward, indicating bubble formation at a fluence of 0.50 $\times$ 10^{20} D m^{-2}. This build-up of gaseous molecules produces increased pressure between the layers of graphite, and eventually, the force of the graphitic layers is less than the force exerted by the gaseous molecules, and a delamination of the graphite layer occurs at a fluence of approximately 1.2 $\times$ 10^{20} D m^{-2}. The second inset reveals the removal of the first layer of graphite, which has become almost completely amorphous in nature.

Complete removal of the first layer is seen, with impacts immediately beginning to modify the second layer and third layer in the same fashion as the first. The final inset shows the process repeating, with modifications above and below the second layer, and some modification to the third layer can be seen.

The swelling of the graphite layers is indicated from Fig 4.6. We place a guideline along the top portion of the data presented in the figure (black, dashed lines) and use the equation generated by that line to produced a value we call the "swelling effect" of the surface as a result of the D impacts. Each D insertion point is then subtracted from this line, effectively removing the swelling from simulation.

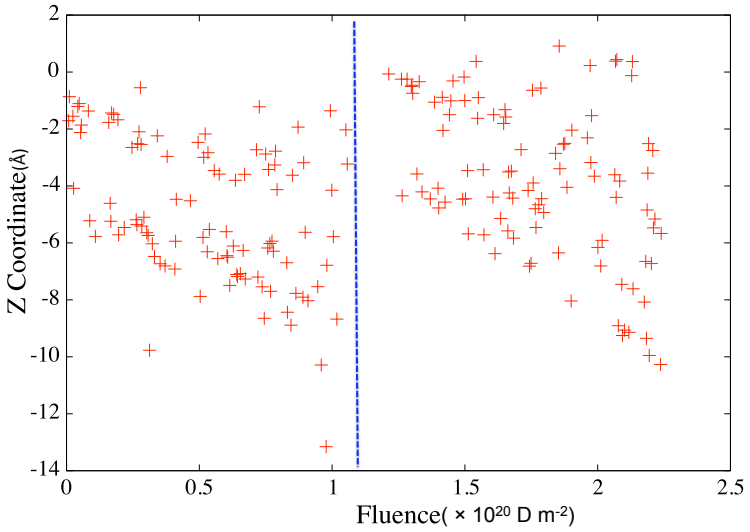

Figure 4.7: Evolution of a graphite system under 20 eV bombardment as a function of time. The Z coordinate value of each point on the black, dashed lines given in Figure 4.6 that coincided with a D insertion was subtracted from the z distance for the given atom. For simplicity, the discontinuity between these is not used for this calculation.

Figure 4.7 shows the results when the data is corrected for the swelling of the system. It is important to note that at the point of delamination in the system is no longer linear due to the rapid removal of the graphite layer, and is not used for the swelling correction. When the data is presented after taking out the swelling effect, a clearer picture of the bubble formation and delamination of the graphite layer is presented. The build up of D atoms on the first two layers is seen from a fluence of 0.0 to 0.5 $\times$ 10^{20} D m^{-2}, with D atoms appearing at -2.0 Å and approximately -6.0 Å. While it is possible that these D atoms do not stay within the bubble during its formation, they do contribute to the overall formation of the bubble and to the delamination of the graphite layer. As damage from the D impacts accumulates on the first layer, the widening of the distribution of D atoms along Z indicates the formation of the low density, amorphous region. The appearance of D atoms between -3.0 Å and -6.0 Å from the fluences of 0.5 $\times$ 10^{20} D m^{-2} to 1.0 $\times$ 10^{20} D m^{-2} may indicate the generation of gaseous molecules between the layers, where we expect the bubble formation to occur. After the delamination event (indicated by the blue, dashed line in Figure 4.7, the process repeats, where damage begins to accumulate on the second and third layers. From fluences of 1.5 $\times$ 10^{20} D m^{-2} to 2.2 $\times$ 10^{20} D m^{-2}, evidence of gaseous molecules between the second and third layer begins to appear. Although a delamination of the second graphite layer is not observed, it is possible another bubble could form and a delamination event could occur if the second and third layer lacks any cross-link formation.

A second histogram is generated using the corrected data. Figure 4.8 shows a tightened distribution of impacting D atoms. This tightening can be attributed to the swelling correction.

When comparing the two graphite systems with 20 eV and 80 eV impact energies, we see a different picture of the formation of the bubble. In Figure 4.9, the impacts are entering from the $+z$ direction. Even in the earliest stages of the simulation, at a fluence of 0.127 $\times 10^{20}$ D m^{-2} (red line), the first two layers of graphite have already lost approximately 42 % of the carbon density compared to the sixth, unmodified layer, and approximately 30 % of the carbon density in the third and fourth layers. This is due to the swelling of the graphite surface and amorphization of the individual graphite layers. At a fluence of 0.56 $\times 10^{20}$ D m^{-2} (green line), the first three layers have lost nearly 75 % graphitic character, and the fourth layer has lost approximately 55 % graphitic character. At the same time, the D density is building up throughout the first four layers of the graphite system, as seen in Figure 4.10. When the system reaches a fluence of 1.41 $\times 10^{20}$ D m^{-2}, the delamination event has not yet occurred, but a large build-up of D density is seen at 34.0 Å in

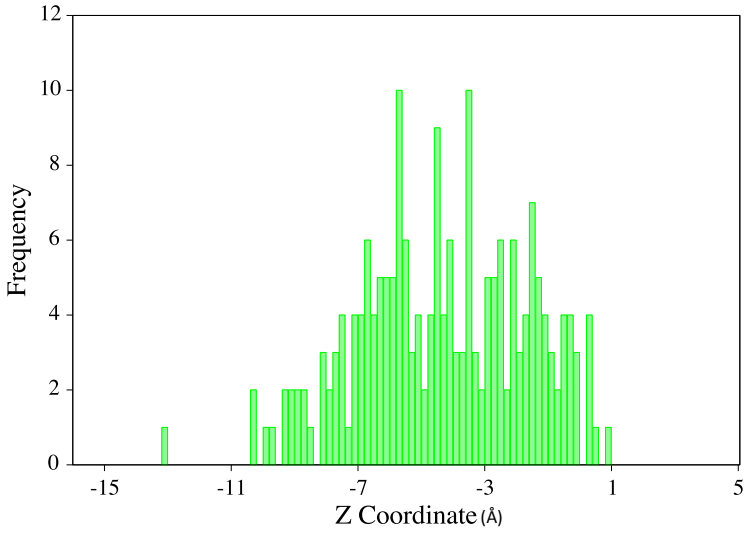

Figure 4.8: The frequency of an inserted D atom in a graphite system 5.0 ps after impact versus the Z coordinate with the swelling correction included. Each unit of frequency counts for one impact, with a total of 365 impacts inserted into the system from time $t = 0$. The energy of the impacting particles is 20 eV.

Figure 4.10. The delamination event occurs at a fluence of 1.6 $\times 10^{20}$ D m^{-2}, between the third and fourth graphite layers, and a portion of the fourth layer has become amorphous by the time this fluence is achieved. Modifications to the lower graphite layers occur at higher fluences, although it is difficult to determine if another bubble will form.

A characteristic of the bubble formation in the 20 eV simulations was a separation formed between layers as a result of gaseous molecule build-up. In the 80 eV simulations, the separation between layers occurs at fluences of 0.56 $\times 10^{20}$ D m^{-2}, much earlier than the delamination event. while D density is accumulated between the first and the third layers (see Figure 4.10) up until the delamination event. The separation between the first and second layers in the 20 eV simulations was easier to determine since the broadening of the density peaks had not yet begun. However, the peak broadening is a more significant factor in the 80 eV simulations.

The contrast to the removal of the graphite layer in the 20 eV system is more stark when comparing the fluences. In the 20 eV system, the fluence only reached a value of 1.02 $\times 10^{20}$ D m^{-2}. The extra time needed to shed the graphite layers from the system could be attributed to the amorphous nature of the layers at the time of delamination. Since the bubble was formed well below the interface of the system and the vacuum and the low density amorphous region is more difficult

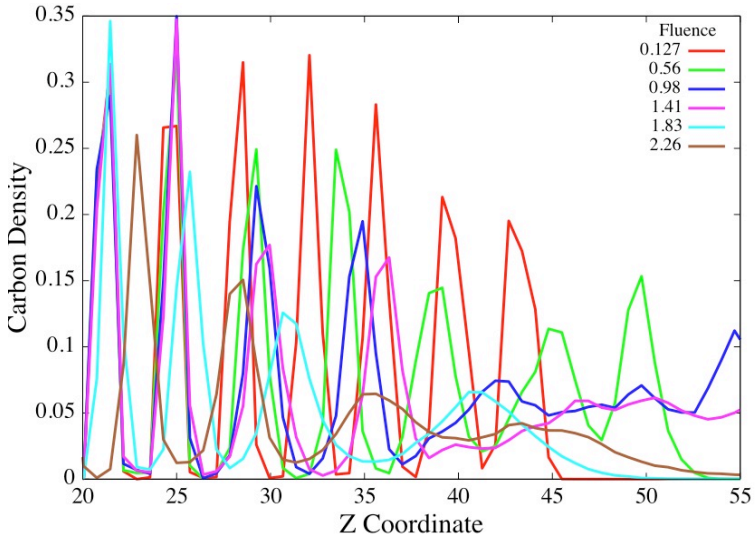

Figure 4.9: Carbon density versus z coordinate for a graphite system under bombardment by D. The impact energy of the inserted particles is 80 eV, and the units given for the fluence is 10^{20} D m^{-2}.

to penetrate through than the graphite layers, which may prevent the initial build-up of gaseous molecules that causes bubble formation.

From Figures 4.9 and 4.10, the early fluence value of 0.127 $\times 10^{20}$ D m^{-2} suggests a penetration depth of approximately 17.0 Å. However, the broadening of the carbon density peaks between the first and third layers, and the amorphization of these layers due to the D impacts, suggests that a penetration depth of nearly 32.0 Å can be achieved at even moderate fluences of 0.98 $\times 10^{20}$ D m^{-2}.

In the same method as the 20 eV simulations, Figure 4.11 depicts a plot of the position of the D atoms 5.0 ps after insertion. A much broader distribution of atom positions is seen than in the 20 eV simulations, meaning the penetration depth is also more varied than the 20 ev simulations, as we've seen previously. A large build up of D atoms occurs near 37 Å, with a portion of the D concentration clustering between 37 Å and 43 Å. This build-up is similar to the 20 eV systems. However, the generation of the modified surface is much deeper, due to the broader penetration depth of the inserted atoms. For the 80 eV impacts, it is more difficult to measure penetration depth with FIgure 4.11. but the retention ratio can be easily measured. By dividing the number of atoms that are in the system 5.0 ps after insertion by the total number of impacts performed, we obtain a retention ratio of 43 %.

Figure 4.12 shows the time evolution of the implanted D atoms in the graphite layers. Here, we can see the penetration depth of approximately 25 Å, while the delamination event occurs at

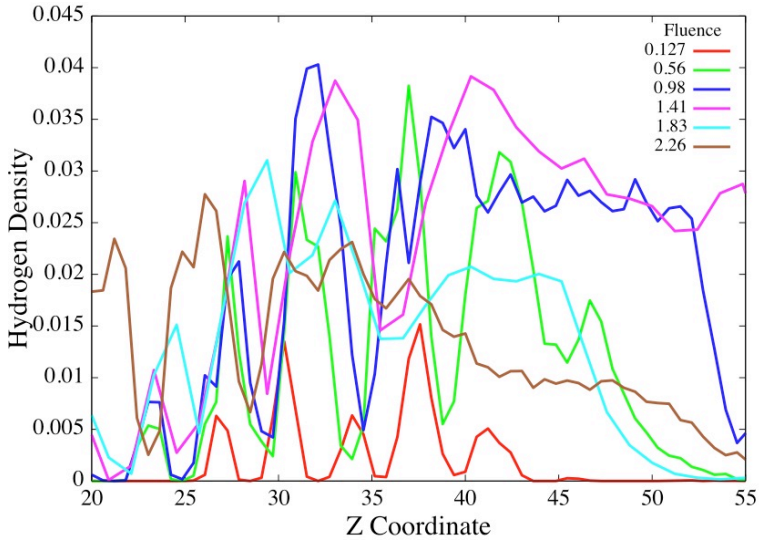

Figure 4.10: Hydrogen density versus z distance for a graphite system under bombardment by D. The impact energy of the inserted particles is 80 eV, and the units given for the fluence is 10^{20} D m^{-2}.

roughly 9 Å below the surface, at 37 Å. From Figure 4.12, the outline of the graphite is shown up to fluences of approximately 0.25 $\times 10^{20}$ D m^{-2}, until the accumulated damage begins to amorphize the first three layers, and some modification of the fourth and fifth layers is seen. The first inset shows the accumulated damage by the D atoms, and the second inset shows the accumulated damage even after the delamination of the first three graphite layers. Unlike the 20 eV system, where most of the damage occurred above the formation of the bubble, significant damage also occurs below the formation of the bubble, and may contribute to the formation of another bubble once the first is removed. The black dashed line indicates the guideline of the graphite swelling as the layers become more amorphous. Figure 4.13 shows the result of the correction for the swelling, in the same method as Figure 4.7.

The amorphization due to the incident D atoms is evident after the a fluence of 0.25 $\times 10^{20}$ D m^{-2} of the simulation, as well as the delamination of the first three graphite layers near 0 Å after taking into account the swelling effect at a fluence of 1.6 $\times 10^{20}$ D m^{-2}. The blue, dashed line indicates the delamination event, and data beyond this line is not corrected.

Figure 4.14 depicts a second histogram of the graphite system under 80 eV bombardment, this time with swelling correction. As in Figure 4.8, the distribution of impacted D atoms is tighter here than in the uncorrected histogram, indicating swelling may be a factor in the initial distribution

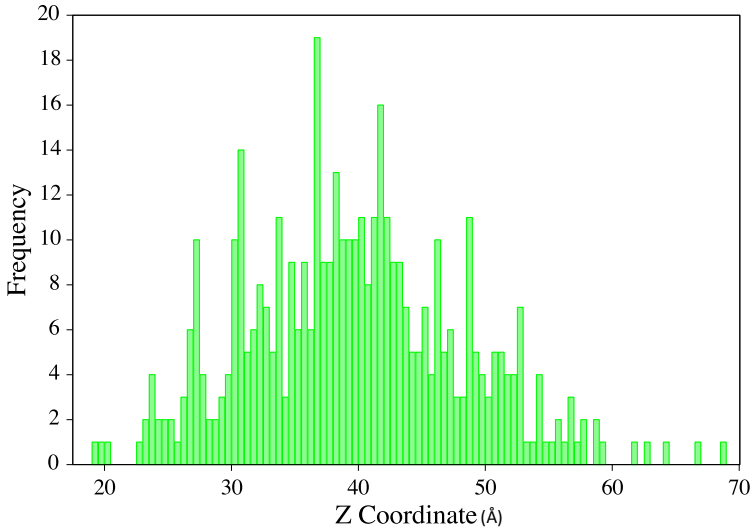

Figure 4.11: Histogram of the frequency of an inserted D or T atom in a graphite system 5.0 ps after impact as a function of Z coordinate. Each unit of frequency counts for one impact, with a total of 1005 impacts inserted into the system from time $t = 0$. The energy of the impacting particles is 80 eV.

4.3.2 Model for Delamination of Graphite Layers

Formation of bubbles in graphite under bombardment by energetic atoms can be studied by the features of the bombardment process, including penetration depth and retention ratio. However, a model based on the number of particles formed inside of the bubble would allow us to gain some understand of when pressure exerted by the bubble would overcome the cohesive force of the graphite layers, and delamination would occur.

Using a pre-constructed eight layer sheet of graphite, the potential energy of the structure was obtained. Then, the eight layered structure was divided into two, four layer sheets of graphite and moved apart from each other by varying amounts. After each distance interval, the potential energy was measured again. The difference in potential energy between the two sheets and the original graphite system was calculated, and plotted in Figure 4.15 as a function of the distances between the two sheets of graphite. The magnitude of the force can be calculated by using a simple one-sided finite difference calculation. This value is the amount of force required to move the graphite layers.

We then determined the amount of outward force exerted by the gas molecules inside of the bubble. At any given point during the simulation, this force can be calculated, given the number of

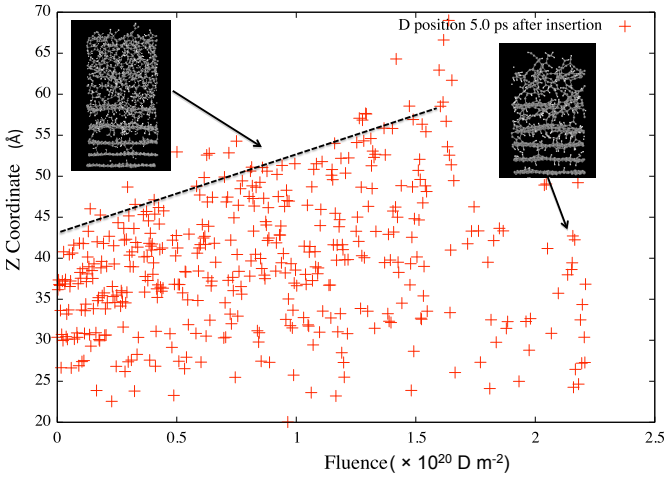

Figure 4.12: Positions of inserted D atoms 5.0 ps after insertion as a function of fluence. The insets are pictures of the system at various times, shown by the arrows. The guideline to account for the swelling effect (black, dashed lines) is used to generate Figure 4.13.

molecules inside of the gas molecules and the separation distance between the two layers where the formation occurs. Starting with the ideal gas law, we have

$$P = \frac{nRT}{V} = \frac{F}{A} \tag{4.1}$$

Where P is the pressure, n is the number of gas molecules inside of the bubble, R is the ideal gas constant, V is the volume, A is the area, and F is the force. Solving for the force, we can simplify the equation into

$$F = \frac{nRTA}{V} = \frac{nRT}{\Delta z} \tag{4.2}$$

Here, Δz is the average z distance between the two layers of graphite in which the bubble forms.

For the ideal gas law, we recognize the limits of the model in the low volume region. From the data in the previous section, we know the bubble forms between the layers of graphite. Using the periodic boundary conditions and the distance between two layers as bounds, we expect volumes to be very small. When the volume of the gas is not negligible when compared with the volume of the container, the pressures given by the ideal gas law tend to be higher than the real pressure of the gas. Also, the intermolecular interactions between the gaseous molecules are not negligible, again

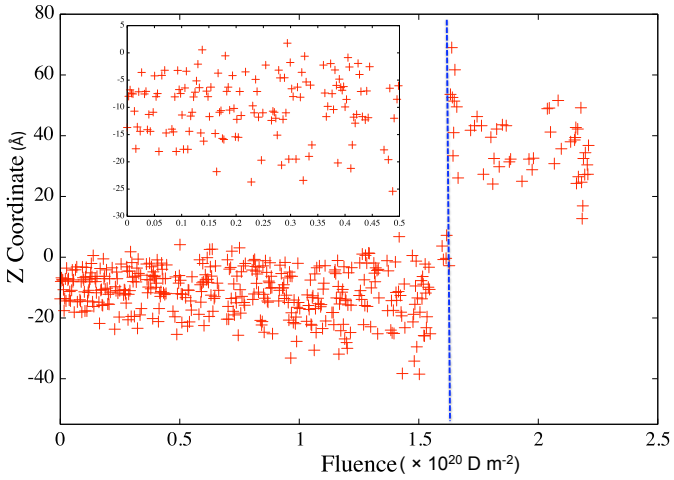

Figure 4.13: Positions of inserted D atoms 5.0 ps after insertion as a function of fluence, with the swelling taken into account. The z coordinate is adjusted by the black, dashed lines given in Figure 4.12. The inset shows a close-up of the data from fluences of 0.0 - 0.5 $\times 10^{20}$ D m^{-2}. The data beyond the blue, dashed line is after the delamination event and is not corrected.

due to the low volumes. Assuming one single gas molecule between the layers forms, pressures are calculated to be 798 GPa. A study performed by Aleksandrov and co-workers[76] tested the limits of graphite structure to 50 GPa. The calculated pressures are an order of magnitude off from high pressure studies performed on graphite.

Regardless, the model does allow for generality. Using the Van der Waals equation for a gas would complicate the model, as the gaseous molecules formed between the graphite layers may not be all of the same type and thus required different coefficients for each differing molecule. Using the ideal gas law as our model allows us to sacrifice some accuracy for generality of the model.

We applied this simple model to our two systems, beginning first with the 20 eV systems. Figure 4.16 depicts the graphite surface within 20 ps of the delamination event which removed the first layer from the system. The seven H_2 molecules used for the calculation are shown with red insets, and there is an average separation of 7.2 Å between the first and second layers, taken from subtracting the difference in z height from a carbon atom in the first graphite layer, and a carbon atom in the second graphite layer. These carbon atoms were in the approximately the same x and y directions. Using Equation 4.2, the total force exerted on the two layers of graphite by the molecules inside of the bubble is 0.12 nN. From the data given in Figure 4.15, the cohesive force between the graphite layers is 0.66 nN. Some of the short comings of the model can be seen from

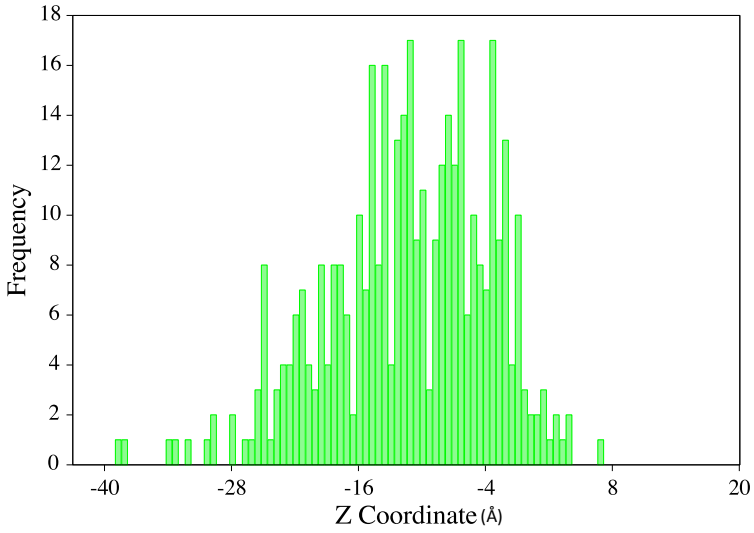

Figure 4.14: Histogram of the frequency of an inserted D or T atom in a graphite system 5.0 ps after impact as a function of Z coordinate, corrected to account for swelling. Each unit of frequency counts for one impact, with a total of 1005 impacts inserted into the system from time $t = 0$. The energy of the impacting particles is 80 eV.

this calculation (described above), however, the model can calculate these forces accurately within an order of magnitude, reasonable for a model based on the ideal gas law.

Figure 4.17 depicts the graphite system bombarded with 80 eV atoms at a point where the bubble will cause the delamination of the top three graphite layers within 20 ps. In the case of the 80 eV simulations, not all of the molecules formed are H_2 molecules. Here, Figure 4.17 shows two CH_2 molecules, a C_2H_2, a CH_4, and a singe D_2 molecules. Using an average seaparation distance of 9.2 Å, the force exerted by the molecules inside the bubble on the amorphous graphite layers is 0.67 nN. At the separation distance of 9.2 Å calculated from the data given by Figure 4.15, the force required to pull the two layers apart is approximately 0.113 nN. The model calculates a much lower cohesive force between the two layers at this distance than the force the gas molecules exert. We speculate this may be due to the formation of a cross-link that has been severed just before the delamination event. This cross-link would increase the cohesive force between the layers, allowing the first three layers to remain tethered to the rest of the surface, even though the force from the bubble is calculated to be much larger than the cohesive force.

Using this model, it becomes possible to make predictive measurements regarding the number of molecules required to separate two graphite layers. In order to make an accurate measurement,

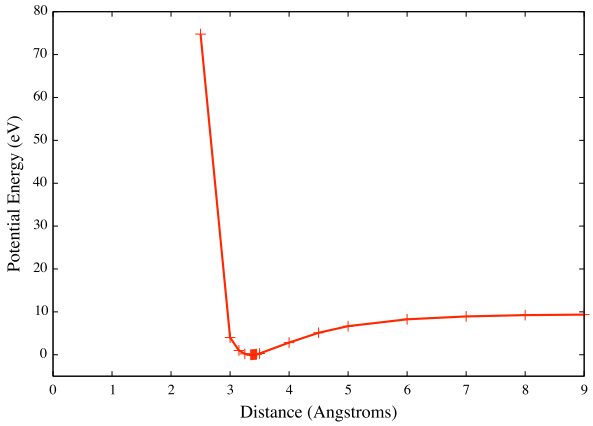

Figure 4.15: Plot of potential energy versus z distance separation between two, four layered sheets of graphite. The slope of this line at any two points (red crosshairs) is the force required to move the sheets over the given distance.

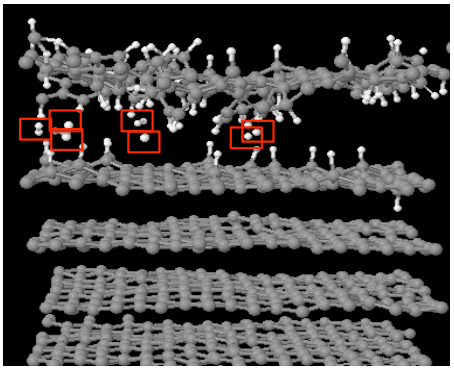

Figure 4.16: The first five layers of graphite after being bombarded wtih 20 eV D atoms. The bubble formation is occurring between the first and second layers (from the top, $+z$ direction. The red squares show the H_2 molecules being used for the force calculation.

the system sizes between those used in the model and the system used to make the prediction would need to be comparable. Based on upon the average Δz distance between the layers and the determined cohesive force, these numbers can be calculated. For example, 14 gaseous molecules would need to be formed between two graphite layers that are an average distance of 3.4 Å apart. This would create a bubble force of 1.4 nN, and start a delamination event, assuming there is no cross-link formation between the layers.

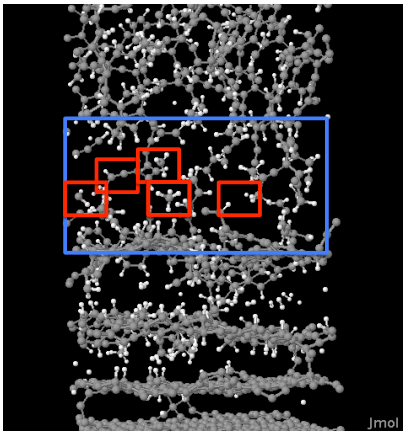

Figure 4.17: First five layers of graphite after being bombarded wtih 80 eV D atoms. The blue square shows the area of bubble formation between the third and fourth layers. The red squares show the molecules being used for the force calculation.

4.4 Conclusions

In this Chapter, bombardment of graphite by atomic D with 20 eV and 80 eV insertion energies was shown to form bubbles between the layers of graphite. While the 20 eV bombardment energies have a well-defined penetration depth, the retention ratio is lower when compared with the 80 eV simulations. The formation of the bubble occurs near the average penetration depth, and our model predicts to within an order of magnitude the force exerted by the gaseous molecules inside of the bubble, providing a possible explanation to the delamination event, where the first layer is completely removed from the simulation.

For the 80 eV simulations, the penetration depth is more broadly distributed, since the more energetic D atoms can penetrate the layers of graphite much deeper. The retention ratio is more than double the 20 eV simulations. It was shown that bubble formation occurs slightly above three layers below the graphite system, with heavy modification of the fourth and fifth layer occurring before and after the delamination of the graphite layer. Our model showed the force exerted by the molecules inside of the bubble was able to overcome the cohesive force of the graphite layers.

It is thought that the simulation conditions themselves may contribute to the formation of bubbles and the delamination of the graphite layers. Because the graphite systems are periodic in the x and y directions, the bubble can persist through the boundary conditions, and the formation of bubbles that are within the boundary conditions is difficult to obtain due to the small system

size. It is also possible that the cohesive force between the graphite layers is also too small when compared to a macro-scale sheet of graphite, and Section 5.2.1 describes the simulations used to confirm this. Chapter 5 investigates this problem by expanding the system in the x and y directions, while adding some additional functionality to the bombardment simulations.

Chapter 5

Improvements and Enhancements to the MD Code for Use in Bombardment Simulations

The reactive potential AIREBO has many powerful supporting features contained within the code. However, there are still many areas within the Molecular Dynamics (MD) code that can be improved to better mimic experimental conditions. The ability to bombard carbon-based systems with multiple atom types with various ratios of atoms has been implemented, allowing the simulation of conditions closer to those found inside of a fusion reactor such as ITER. Additionally, the Langevin thermostat has been allowed to function during the use of the variable time step algorithm. This improvement is key for the ability to model systems that have been doubled in size normal to the bombardment, the x and y directions. As a test with these new enhancements, bombardment on expanded graphite surfaces are performed with a mixture of 50 % D and 50 % T atoms, and results are presented as proof of concept for the enhancements to the code.

5.1 Introduction

Ion-surface collisions are relevant to a wide variety of scientific and technological applications, ranging from astrophysical systems to surface analytical methods and plasma-surface interac-

tions. In particular, impact of hydrogen, especially its heavy isotopes, on carbon-based materials is of relevance for magnetically confined hydrogen fusion plasmas, in which graphitic materials are often used as plasma-facing components, due to their advantageous thermal and mechanical properties, as well as their low atomic number.[11]

Consequently, there has been a great deal of interest in the sputtering of graphite by atomic, ionic, and molecular hydrogen isotopes, much of it at the chemical sputtering energy range between 5 and ∼100 eV.[27;50;51] Previous work has included both experimental[25;27;51–55] and computational[34;35;41;42;49;53–61] approaches, using both monoenergetic beams and plasmas. Similarly, more current approaches[15;16] have focused on starting conditions such as choice of initial surface and potential.

Bombardment of graphite and amorphous carbon surfaces has shown that while surface evolutions and computational studies of these surfaces are good compliment to experiments, some results agree very poorly with experimental outcomes.[25;51;52] These results, such as carbon sputtering over the lifetime of the simulation and evolution of the modified surface, may have large effects on the results of the simulation. Over the course of several generations of simulations[15;16] found in Chapters 2 and 3, flaws in the simulation conditions have made it apparent that additional functionality within MD code is required. As such, some improvements to the simulation conditions have already been used in Chapters 2 and 3, such as exclusive use of the AIREBO potential, and the choice of only graphite as the starting surface.

Other simulations involving the REBO and AIREBO potential have also run into contention with experimental conditions[77]. These discrepancies can often lead to unphysical changes seen in the simulation that are not observed in the experiment, such as excessively large carbon yields[16]. These differentiations from experiment can largely be explained by the starting conditions and other factors that are necessarily involved in the simulation conditions. This work details changes made to the MD code that allow for closer comparison to experimental conditions.

5.2 Computational Details

In the simulations performed, two graphite surfaces were bombarded by a mixture of 50 %D and 50 %T atoms at two different insertion energies, 20 eV and 80 eV. The AIREBO potential was used to perform dynamics on these systems.

The graphite system comprised of 5,760 atoms in eight layers. Periodic boundary conditions were imposed in the two Cartesian dimensions parallel to the graphite layers, with box lengths of 44.30 Å and 42.62 Å. The graphite layers were initially separated by 3.35 Å, resulting in a system size of 26.8 Å in the direction perpendicular to the graphite layers, which we label z. The system size was free to change in this direction, as periodic boundary conditions were not applied. Periodic boundary conditions perpendicular to z, in the x and y direction were applied. The graphite system was equilibrated to 900 K using a Langevin thermostat before beginning bombardment. Similar to Chapter 4, the focus of this work is the improvements made to the MD code, and while the temperature dependence will not be discussed, the ability to perform NVT dynamics with the variable time step algorithm will be explained here.

5.2.1 Thermostat and Variable Time Step

As mentioned previously in Chapter 4, the second generation of graphite simulations at 900 K produced some interesting results. Void, or bubble, formations were seen by two different systems, one using 80 eV impact energies, and the other using 20 eV impact energies. The formation of the bubble is dependent on the impact energies due to the variation in penetration depths and retention ratios. While the process of the bubble formation and delamination of the graphite layers is known, the simulation conditions may be problematic.

Previous work involved serial bombardment of 20 eV D atoms were performed on graphite systems using the AIREBO potential seen in Chapter 2. After achieving a fluence of approximately 2.0×10^{20} D m^{-2}, the total potential energy of the system was calculated. Then, the first layer of the graphite sheet was removed from the system, and the potential energy for this layer and the set of seven layers was calculated individually. The difference in potential energy between these two layers is the binding energy of the first graphite layer to the rest of the graphite surface, and was found to be approximately 10 eV, or half the energy of the 20 eV insertions, and only an eighth of the energy of the 80 eV insertions. This result indicates that if no cross-links form between the damaged layer and the rest of the system, a single D insertion would have enough energy to delaminate the entire layer. The formation of bubbles between the graphite layers as in Chapter 4 would only decrease the amount of energy needed for the delamination to occur as the pressure exerted by the bubble on the graphite layers increases.

To determine if the void formation discussed in Section 4 is a result of the simulation

conditions proposed in Chapters 2, 3, and 4, an expansion of the graphite layers in the x and y direction is used. This increases the simulation area of graphite by a factor of four. In order to keep the flux the same as in previous simulations, the rate of insertion of a particle into the simulation is increased by a factor of four as well. If the same computational methods were used as in the previous generation of simulations found in Chapters 2, 3, and 4, the Langevin thermostat would need to be turned on every 1.0 ps for a duration of 0.5 ps. Since this duration is within the region of multiple bond breaking and bond formation activity where the dynamics of the simulation would be most sensitive to a thermostat (described in Section 2.3.1), the use of a thermostat to model NVT dynamics with the variable time step algorithm would be beneficial. However, a restriction in the MD code allows only static time steps during NVT dynamics. It has been shown in Section 2.3.1 that a wide range of time steps are often needed to model the dynamics of the insertions while still maintaining reasonable energy conservation.

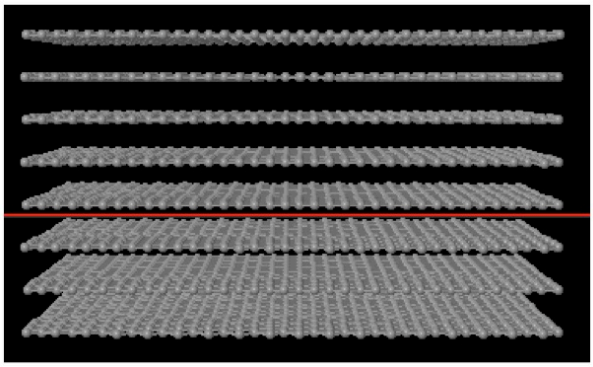

Figure 5.1: Schematic of a clean graphite surface with dimensions of 44.30 Å in x, and 42.63 Å in y. The solid red line indicates a zone boundary, where above this line, in the $+z$ direction, the system is treated with no Langevin thermostat. Below the red line, in the -z direction, the system is treated with a Langevin thermostat at 900 K. Below the line corresponds to the bottom three layers of the graphite system.

Computationally, implementation of a variable time step while the thermostat is on is accomplished in a similar method to the implementation of the actual variable time step algorithm, described in Section 2.3.1. The integrator takes a step using the previously accepted time step with no atoms in the simulation subjected to the Langevin thermostat. If the energy tolerance (see Section 2.3.1 is below the acceptable D_E range, then the time step is accepted. At this point, the simulation is rewound back to the previous time, and taken once more with the Langevin thermostat initialized and the accepted time step. If the energy tolerance is above the D_E range, the time step

is rejected, the simulation is wound back to the previous, accepted time, and a smaller time step is used.

In experimental conditions, the graphite sheets used within ITER reactors and in beam experiments are composed of many layers of graphite, far more than the eight used in our simulations. The energy transferred after insertion of an incident particle, and the subsequent temperature increase is allowed to disperse through an area that is many times greater than we can simulate. The thermostat can be used as a substitute for these many layers, effectively removing excess thermal energy of the incident particle.

The position of the thermostat in these larger systems is different from the previous generation of simulations.[15;16] Figure 5.1 shows the position of the zone interface. Above this interface, all atoms are free to move according to NVE dynamics, and are not subjected to a thermostat. Below this line, atoms are subjected to a thermostat of 900 K continuously. This setup is also arguably closer to the experimental system described above, where the graphite system is larger in directions perpendicular to the impact region. Also, the zone where the thermostat is applied is well below the impact region, simulating the "bulk" character of the graphite. Here, heat generated by the impacting particle and its affect on the surface will disperse naturally to the thermostated region as the fluence increases.

Since there were 1.0 ps of dynamics between impacts, the nominal flux at which the bombardment was performed for graphite was 5.3×10^{28} D m^{-2} s^{-1}. This is many orders of magnitude larger than experimental fluences, which will only reach $\sim 10^{25}$ D m^{-2} s^{-1} even in large fusion reactors such as ITER. The incorporation of the thermostat that is always on functions as a heat bath, lowering the effective flux of the simulation.

5.2.2 Bombardment with Multiple Atom Types

Experimentally, damage that occurs to the divertor plates in reactor such as ITER is often from a source of mixed D and T particles. These particles are often charged as well, due to the high-energy plasma. While we do not have the capacity to model charges with the current version of the MD code, the ability to bombard surfaces with multiple atom types has now been implemented. When setting up a sputtering simulation, multiple files are required to set the simulation conditions. One of these required files, the .sput file, specifies key parameters of an inserted atom such a insertion plane, incident kinetic energy, and flux of the incident atom. The previous version of the .sput file,

labeled version four, contained a single line specifying the file name and location of a single inserted species. In the new version of the file, labeled version 5, and additional line of code was added, this time specifying the number of different file names, which correlate to the number of atom types inserted (line two in the pseudocode below).

For example, if a mixture of D and T atoms were to be inserted, the first field of line two would be set as "2'." Then, for each atom type, the file names and locations of the selected species must be specified (the first field of lines three and four). The second field of the third and fourth lines specify the ratio of the inserted species. The total value of the second field in the third and fourth lines must be equal to 1.0. If the value is greater than or less than 1.0, the simulation will produce an error and not start.

```
5                  # .sput file version number
2                  # number of atom types to be inserted
'./d.coord' 0.5    # file #1 containing inserted species
'./t.coord' 0.5    # file #2 containing inserted species
```

Once the parameters within the .sput file are specified, the simulation is started. To determine which of the selected species is inserted, random number between 0.0 and 1.0 is generated. If this random number is within the given ratio of first specified species, that species is inserted. If the random number is not within the given ratio of the first specified species, the sum of the second field in the first and second species is compared to the random number. If this value is within the random number chosen, a T atom is inserted. This process continues if there are more than two species in to be inserted. Any ratio of any number of species can be specified by adjusting the second line of the pseudocode above, and adding species until the ratio of the selected species is 1.0 (to a maximum of 12 different species).

Using this improvement to the MD code, each surface was bombarded sequentially with D/T impacts, reaching total fluences of up to 0.17 $\times 10^{20}$D m^{-2} for the graphite AIREBO system. Any reflected or sputtered species were removed from the simulation cell once they reached a distance of approximately 30 Å above the interface with a center-of-mass velocity directed away from the surface; this criterion was adjusted to account for swelling of the substrate, so that particles were only removed once they were no longer interacting with the substrate.

5.2.3 Results of the Large Graphite Simulations

To determine if the improvements made to the MD code outlined in Section 5.2 are implemented properly, sequential bombardments were performed. Figure 5.2 shows the damage accumulated on the graphite surface after serial bombardment of 20 eV D/T atom mixture. The particles are being inserted into the system correctly and with the correct energies. The thermal fluctuations noticed in the upper six layers of graphite in Figure 5.2 indicate that NVE dynamics are being performed.

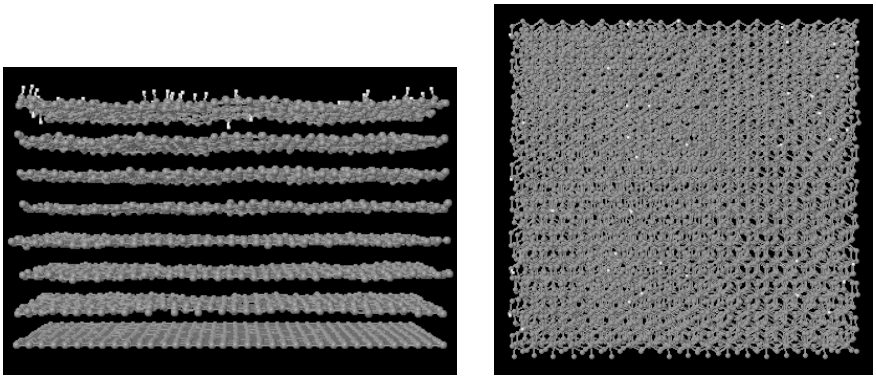

Figure 5.2: Side profile (left panel) and view from the $+z$ direction (right panel) of a graphite surface after a fluence of 0.17 $\times 10^{20}$ D m^{-2} is reached with a 20 eV mixutre of 50 %D and 50 %T atoms. Here, the thermostat region is contained within the

For these simulations, we note that impacts are produced every 1.0 ps, instead of every 4.0 ps as in Chapters 2 and 3. At every time step where an insertion takes place, the energy conservation check is skipped for that time step. The energy conservation may appear poor at first glance, but upon closer inspection, nearly all of the energy increase comes from the thermal energy deposited by the impacting particle (i.e kinetic energy). The energy increases until a fluence of 0.04 $\times 10^{20}$ D m^{-2}. This corresponds to approximately 80 impacts. At 20 eV per insertion, approximately 1600 eV of energy has been inserted into the system. The total energy increase is nearly 500 eV over the same fluence, according to Figure 5.3. As the D atoms impact the surface, their kinetic energy is transfered to the surface. The process of bond breaking and formation begins once the impacting atom has transferred enough energy to cause a bond formation event. Once the thermal energy has transferred through the layers to reach the thermostat region, or the number of C-H bonds being formed outweighs the energy inserted every 1.0 ps into the simulation, the energy begins to decrease.

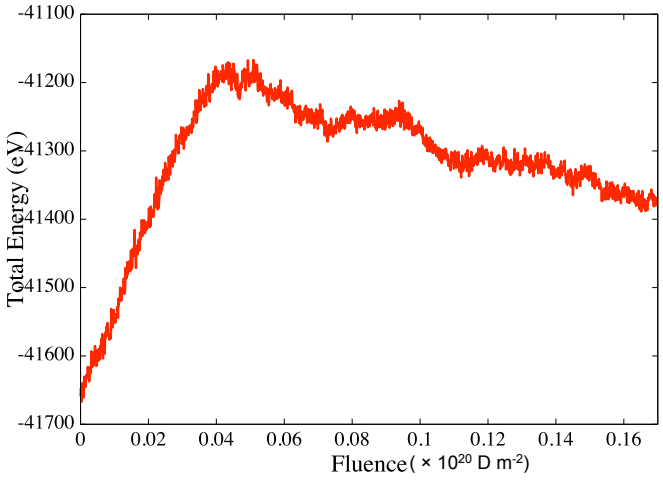

Figure 5.3: Total energy plotted as a function of fluence for a graphite system expanded in the x and y directions and subjected to 20 eV impacts of mixed 50 % D and 50 % T atoms, with an energy of 20 eV.

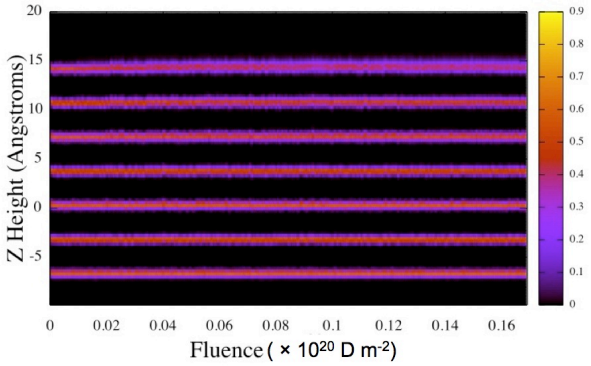

Figure 5.4: Carbon density plot in the z direction of a graphite system bombarded with a 20 eV mixture of 50 % D and 50 % T atoms. The impacts are normal to the surface, from $+z$, and the fluence is given in units of 10^{20} D m^{-2}

Figure 5.4 is a carbon density map of the graphite system, where impacts are coming from $+z$ direction. Because the rate of impacts has been increased four-fold to match the four-fold increase in area, the fluence values are comparable to previous simulations (see Sections 2 and 3 for further details). Although at these low fluence values it is difficult to compare the results of the surface evolution, the integrity of the first layer of graphite is mildly compromised at a fluence of 0.14 $\times 10^{20}$ D m^{-2}, with a very mild broadening of the carbon density peak seen at that fluence.

To continue the test of the enhancements of the MD code, the same graphite surface used

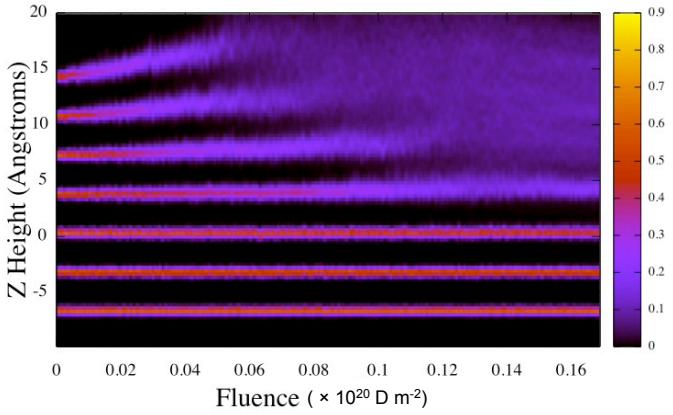

Figure 5.5: Carbon density plot in the z direction of a graphite system bombarded with a 80 eV mixture of 50 % D and 50 % T atoms. The impacts are normal to the surface, from $+z$, and the fluence is given in units of 10^{20} D m^{-2}.

for the 20 eV impacts was bombarded with an 80 eV mixture 50 % D and 50 % T atoms. Figure 5.5 shows the results of the early bombardments. Even at low fluence values, the damage done to the graphite layers is extensive, with the integrity of the first four layers being compromised before a fluence of 0.08 $\times 10^{20}$ D m^{-2}., in roughly half the time it takes the 20 eV simulations to begin to show evidence of wear. The layers become amorphous in character, with multiple cross-links, or bonds between graphite layers, being formed between them.

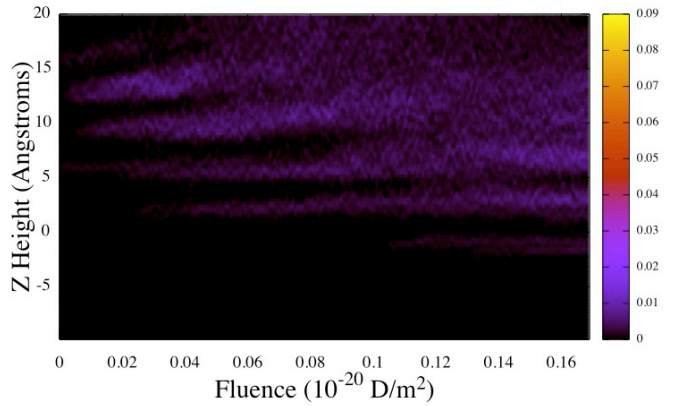

Figure 5.6: Hydrogen density plot in the z direction of a graphite system bombarded with a 80 eV mixture of 50 % D and 50 % T atoms. The impacts are normal to the surface, from $+z$, and the fluence is given in units of 10^{20} D m^{-2}.

Figure 5.6 shows the distribution of combined D/T density of the system as the fluence increases. While the majority of the D/T atoms are deposited in the first four layers, some of the D/T atoms become embedded in the fifth layers at a fluence of 0.16 $\times 10^{20}$ D m^{-2}. The first and second layers begin to form cross-links and become amorphous at 0.08 $\times 10^{20}$ D m^{-2}. While this shows the 80 eV simulations are able to evolve graphite with sequential D/T bombardment, the energy conservation of the system also needs to be evaluated.

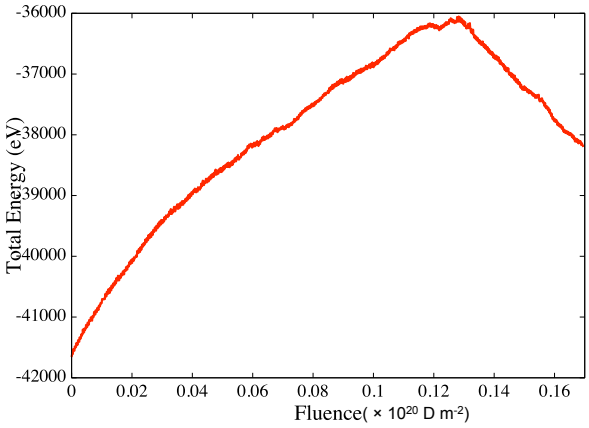

Figure 5.7: Total energy plotted as a function of fluence for a graphite system expanded in the x and y directions and subjected to impacts of mixed 50 % D and 50 % T atoms, with an energy of 80 eV.

Figure 5.7 shows the total energy of the graphite system versus time. As with the 20 eV simulations, the 80 eV simulations show a steady rise in total energy as the energy is deposited from the 80 eV impacts. After the first four layers become mostly amorphous, and the fifth layer has accumulated some damage, the energy drastically decreases. This could be explained by the formation of the cross-link (Figure 5.9 between the lowest layer that is free of thermostat control and the first layer that is under control of the thermostat. The cross-link acts as a conduit of heat transfer between the graphite layers, and allows for thermal energy to flow to the thermostat zone in a much more efficient manner. This is explained by the fact that the thermal conductivity of in-plane graphite is roughly two orders of magnitude higher than out-of-plane graphite[78]. Figure 5.8 shows the drastic temperature decrease as the cross-link is formed.

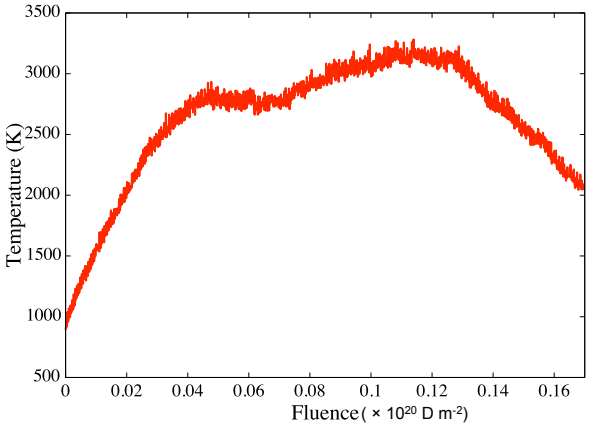

Figure 5.8: Temperature plotted as a function of fluence for a graphite system expanded in the x and y directions and subjected to impacts of mixed 50 % D and 50 % T atoms, with an energy of 80 eV

After a fluence of 0.17 $\times 10^{20}$ D m^{-2} had been achieved through bombardment, an examination of the carbon and hydrogen densities was performed. Figure 5.10 shows substantial decrease of the carbon density of the first three layers (red, solid line) compared to the undamaged layers, and merging of the three layers into one broad peak to form an amorphous structure. The D density (blue, dashed line) is increased by an order of magnitude in the figure for ease of viewing, but shows increasing density in the same region of the break down of the carbon density peaks. The D/C ratio in this broadened region of the carbon density is 0.025 on average. At these low fluences, it is difficult to determine the final amorphous structure in terms of D and C density as more impacts are needed to evolve the graphite surface to its final steady state.

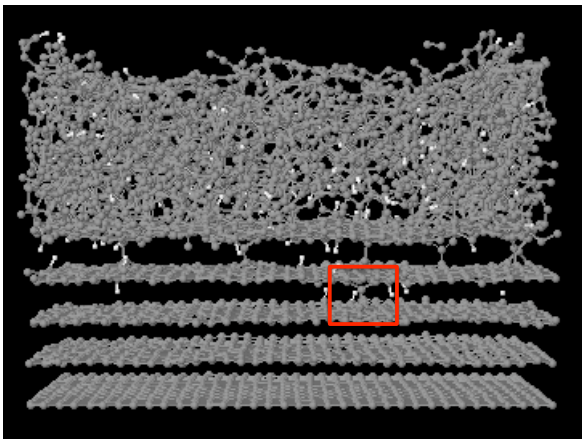

Figure 5.9: Graphic of a damaged graphite system after being sequentially bombarded with a mixture of 50 % D and 50 %T atoms. The energies of these atoms was 80 eV. The red inset shows the cross link formation between the zones with no thermostat and the zones with a thermostat.

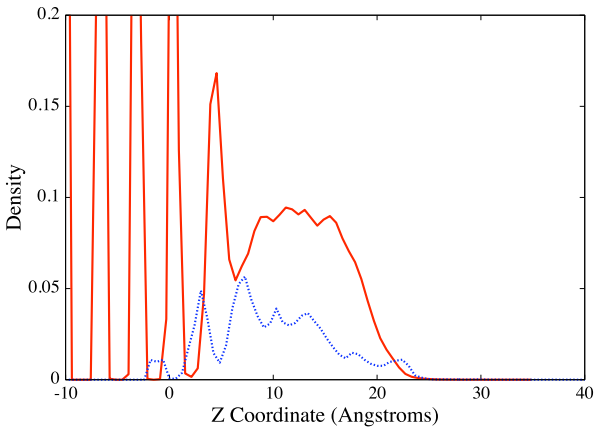

Figure 5.10: Carbon density (red, solid line) and deuterium density (dashed, blue line) of the expanded graphite surface after 80 eV bombardment at a fluence of 0.17 $\times 10^{20}$ D m^{-2}. For clarity, the hydrogen density has been increased by an order of magnitude.

5.3 Conclusions

While the AIREBO potential is useful and accurate for modeling a variety of hydrocarbon systems, some functional improvements to the MD code are required to better simulate experimental

conditions. Improvements such as the use of the variable time step algorithm while having the thermostat turned enabled, and the ability to bombard a system with multiple atom types are employed as enhancements to the code. As a result, graphite systems were doubled in the x and y directions to better simulate a larger graphite surface, and were bombarded with 20 eV and 80 eV D and T atoms, as a test for the additions added to the MD code. It was found that systems behaved mostly as expected for these larger systems operating under different simulation conditions, but further impacts and additional analysis are necessary to gain a more complete understanding of the surface evolution with these enhancements.

Chapter 6

Conclusions and Final Thoughts

In this work, we have presented MD simulations of graphite and amorphous carbon surfaces under serial bombardment by energetic deuterium atoms and it isotopes. The surfaces evolved based on a number of factors, including choice of starting surface, potential, temperature, and bombardment energies. From the previous chapters, we have attempted to optimize simulation conditions to better mimic experimental conditions currently in use, such as beam experiments of the tokamak reactor ITER.

It was found that choice of starting material was crucial to the outcome of the simulation. When comparing two surfaces, graphite and amorphous carbon, the graphite surface evolved differently than the a:C-D surface in terms of carbon density changes, and the evolution of the steady state. This may be due to the characteristics of the system itself. The ordered, eight layer graphite is only a single atom thick between sheets. The a:C-D system, however, is a dense network of disordered deuterium and carbon atoms. It was shown that unlike the initial assumption, where graphite and a:C-D systems would both reached the same steady state, needed to be modified. The choice of starting surface can have a large impact on the steady state, with graphite exhibiting cyclical steady state generation, while a:C-D systems showed a gradual decline in density and a different D/C ratio when reaching the steady state.

The choice of potential was also examined. It was found that the long ranged interactions of AIREBO were needed to better model the surface. The torsional and Lennard Jones terms played a key role in the surface evolution. In addition to potential choice, the modeling of the thermostats were also important in the MD simulations. Rather than enabling the thermostat for the entire

system, including the portions close to the graphite system and vacuum interface, "zones of control" were enabled to thermostat only the portion of the system that was still contained much of the original carbon density. This was done to prevent unnecessary build-up of the low density amorphous carbon region. While this region may persist even in the newest generation of simulations, the new thermostat zoning method represents a step toward a better model of experimental conditions.

The formation of bubbles in graphite systems as a result of energetic bombardment can be described by a the penetration depth of the particles, and the retention ratio, which may cause bubbles to form earlier if the retention rate is higher. By using a predictive model based on the ideal gas law, the number of molecules and the separation between the layers can determine whether the force inside the bubble is greater than the cohesive force between the bubbles.

To test whether the simulation conditions are a possible cause of bubble formation, the graphite systems were expanded in the x and y directions, allowing the cohesive force between the graphite layers to multiply by a factor of four. Along with this change, the bombardment of multiple atom types within the simulation was also implemented, coming closer to experimental conditions. Furthermore, the thermostat functionality was also expanded to function with the variable time step theorem, allowing the use of alternate time steps for the duration of the simulation. The simulations are early into their evolution but are already exhibiting interesting properties.

We have presented several recommendations and enhancements to the MD code that have shown to improve the simulation conditions for bombardment of graphite and amorphous carbon surfaces and have allowed us to more closely model experimental conditions than in the past. With these changes, greater comparison to experiments can be made, and simulations can further be improved.

Appendices

Appendix A Enhancements to the LAMMPS Code

A.1 Introduction

Recently, the AIREBO potential has been implemented in the parallel LAMMPS package. Along with the ability to run in parallel, LAMMPS offers several other important improvements, such as updated coding language and ease of expansion. This is mostly due to the inherent separation of the parallel architecture from the potential implementation in the package. However, several users have pointed to inherent flaws within the AIREBO code residing in LAMMPS. These flaws range from poor energy conservation to unphysical NVE dynamics in the graphite layers. The following changes, enhancements, and bug fixes detailed below have been released as full patches to the publicly available LAMMPS source code.

A.2 Computational Details of LAMMPS Comparison

An amorphous carbon system with a D/C ratio of 0.4 was used to evaluate the integrity of the AIREBO implementation in LAMMPS, as shown Figure 1.1 (right panel). Periodic boundary conditions were employed in the x and y directions in a similar fashion as Fallet *et. al.*, with periodic boundaries turned off or extended beyond the cutoff range in the z direction. For purposes of this experiment, inital temperature, and velocities are disregarded. The entire system is set up in an NVE environment, with no modifications or thermostats included.

Initial energy comparisons were made between original source AIREBO potential and its implementation in LAMMPS on a deuterated amorphous carbon (a:C-D) system. A section of the a:C-D system was then randomly spliced and compared once again. If this spliced system showed an energy inconsistency, it was further spliced. Using this "drill-down" approach, the system can be cut into increasing smaller sizes that still contain the energy discrepancy. Once the system cannot be spliced any further to contain the energy error, the individual bonds of the small system are dissected into their component energies, and comparisons continue until the energy discrepancy is found. Listed within these changes are the approximate impact each change has on the total energy of the a:C-D system. The original AIREBO source code gave the total energy of the a:C-D system to be -13,821.401 eV, while the total energy in the LAMMPS code was found to be -13,827.609 eV.

A.3 Decimal Corrections

The REBO portion of the AIREBO potential, developed by Brenner,[8] contains three terms, the bond-order b_{ij} term, a repulsive V^R term, and an attractive V^A term. These three terms are shown together in Equation 1.11. The V^R and V^A terms are given by Equations 1.12 and 1.13, respectively. These parameters (including π) were given 8 digit precision in the LAMMPS code. However, the AIREBO code permits 16 digit precision. The corrected values are given in Appendix A.7.

Within the b_{ij} term referenced in Equation 1.14 are the $p_{ij}^{\sigma\pi}$ and $p_{ji}^{\sigma\pi}$ terms, which depend on the local coordination number and the chemical environment of the bond. There is another contribution, π_{ij}^{rc}, that includes contributions from the radical character of the bond, which is evaluated as a three dimensional cubic spline function. The values for the coefficients of the three dimensional cubic spline discussed in Section A.3 are given values of N_{ij}, N_{ji}, and N_{ij}^{conj}. The first two values, N_{ij} and N_{ji} are coordination numbers, while N_{ij}^{conj} is a local measure of the conjugation of the $i-j$ bond. These coefficients, or interpolation points on which this spline is evaluated were increased to 16 digit precision, and are listed as i, j, and k, respectively, and are given in Appendix A.8. These corrections resulted in a net of approximately 0.1 eV in the total energy discrepancy between the two potentials.

A.4 Additions and Omissions

The transcribed AIREBO code within LAMMPS was based off of the values written in Stuart, *et. al.*[9]. During the conversion of the code from C++ to Fortan, some values were changed or omitted. The corrected values are listed below. These corrections resulted in a net of approximately 0.1 eV in the total energy discrepancy between the two potentials.

```
piCCdfdz[1][1][2] = -0.0302715;
piCCdfdy[3][1][2] =  0.018772388;
```

A.5 Revisions

In the original AIREBO code published by Stuart *et. al.*[9], the boundaries of the three dimensional cubic spline were listed as (0-3), (0-3), and (0-9) for the values of N_{ij}, N_{ji}, and N_{ij}^{conj}, respectively. In order to avoid unlikely but plausible scenarios of these values going above their intended maxima, the "top end" was extended by an additional digit. Although for most chemical systems, the maximum coordination number for a carbon atom is four, there exists some transition states where a bond may be in the process of formation between two atoms, which will manifest by exhibiting a coordination number greater than four. The value of the top end is the same value as the maxima, meaning

$$N_{ij}^{3} = N_{ij}^{4} \tag{1}$$

$$N_{ji}^{3} = N_{ji}^{4} \tag{2}$$

$$N_{ij}^{conj(9)} = N_{ij}^{conj(10)} \tag{3}$$

This equality was not carried over into the LAMMPS implementation of AIREBO, and was stated to be zero instead of the top end value. This has been revised in the current generation of the LAMMPS package. Computational details of this change can be found in Appendix A.9. In addition, the upper bounds of these variables were also incorrectly set, and this minor but important change has been detailed in Appendix A.12. These corrections resulted in a net of approximately 1.0 eV in the total energy discrepancy between the two potentials.

The LJ interaction of the AIREBO portion of the potential is adaptively turned on or off, depending on the chemical environment. The full equation for the LJ interaction is given by

$$E_{ij}^{LJ} = S(t_r(r_{ij}))S(t_b(b_{ij}^{*}))C_{ij}V_{ij}^{LJ}r_{ij} + [1 - S(t_r(r_{ij}))]C_{ij}V_{ij}^{LJ}(r_{ij}) \tag{4}$$

For a full explanation of terms, see Stuart *et. al.*[9]. Here, the b_{ij}^{*} term is subtly different than the b_{ij} term found in the REBO potential (Equation 1.11). This is a hypothetical b_{ij} term, evaluated at the minimum REBO cutoff distance, since the adaptive LJ interaction is evaluated for

intermolecular distances, which exceeds the covalent bonding separation of r_{ij}^{max}, thus

$$b_{ij}^{*} = b_{ij}|_{r_{ij}=r_{ij}^{min}} \tag{5}$$

In the AIREBO source code within LAMMPS, this imaginary cutoff was incorrectly set to the *actual* r_{ij} REBO distance, causing an energy discrepancy. It is also believe, but not fully tested, that this also caused some force evaluations to be incorrect. Within the LAMMPS code, the variable called *rij0mag* is the actaul r_{ij} distance, which is being set to the imaginary distance *rijmag* in the pseudpcode below, along with the vector distances. Uncommenting these lines results in a next change of approximately 4.0 eV in the total energy discrepancy between the two potentials.

```
rij[0] = rij0[0];
rij[1] = rij0[1];
rij[2] = rij0[2];
rijmag = rij0mag;
```

The E_{ij}^{LJ} energy mentioned in Equation 4 is modified by many splines and cut-off functions. In the original AIREBO source, the LJ interaction is smoothly turned off after the r_{ij} distance is greater than the cutoff distance, r_{ij}^{LJmax}. This cutoff function, originally not included in the LAMMPS implementation, has been added. Details of the implementation can be found in Appendix A.10.

A.6 Bug Fixes

The b_{ij} term in the REBO potential, as seen in equation 1.14, contains the $p_{ij}^{\sigma\pi}$ terms, which is the covalent bond interaction. This interaction is given by

$$p_{ij}^{\sigma\pi} = [1 + \sum_{k\neq i,j} w_{ik}(r_{ik})g_i(cos_{ijk})e^{\lambda_{ijk}} + P_{ij}]^{-\frac{1}{2}} \tag{6}$$

The P_{ij} term is a two dimensional cubic spline function, in part used to reproduce accurate bond energies for small hydrocarbon systems. The bounds for this spline were incorrectly set in the LAMMPS code, and the corrected values for the boundaries are given in Appendix A.11.

The function g_i imposes a penalty on bonds that are too close to one another. When the central atom is a carbon, the spline depends on the local coordination number, which is the sum of the carbon and hydrogen only coordination numbers. Here, it is important to note that the local position of the atoms as the energy is calculated is positional dependent, and if the first atom studied is a hydrogen, the interaction of N_{ij}^{C} is zero. The LAMMPS implementation of AIREBO did not account for this, and the change is detailed in Appendix A.13.

A.7 Decimal Corrections

```
PI = 3.14159265358979
0.3134602960832605     Q_CC
0.3407757282257080     Q_CH
4.746539060659529    alpha_CC
4.102549828548784    alpha_CH
10953.54416216992    A_CC
149.940987228812    A_CH
12388.79197798375    BIJc_CC1
17.56740646508968    BIJc_CC2
30.71493208065162    BIJc_CC3
32.35518665873256    BIJc_CH1
4.720452312717397    Beta_CC1
1.433213249951261    Beta_CC2
1.382691250599169    Beta_CC3
1.434458059249837    Beta_CH1
0.7415887    rho_HH
0.0028437324 epsilon_CC
0.0020639767 epsilon_CH
0.0014994226 epsilon_HH
0.3078851086 epsilonT_CCCC
0.1786600912 epsilonT_CCCH
0.1249753356 epsilonT_HCCH
```

```
0.370     Q_HH
3.536                alpha_HH
31.6731    A_HH
28.2297      BIJc_HH1
0.0          BIJc_HH2
0.0          BIJc_HH3
1.708        Beta_HH1
1.0          Beta_HH2
1.0          Beta_HH3
0.0014994226 epsilon_HH
2.65         sigma_HH



PCCf[0][3] = 0.0161253646
PCCf[1][1] = -0.010960;
PCCf[1][2] = 0.00632624824;
PCCf[2][0] = -0.0276030;
PCCf[2][1] = 0.00317953083;

PCHf[0][1] = 0.209336733;
PCHf[0][2] = -0.0644496154;
PCHf[0][3] = -0.303927546;
PCHf[1][1] = -0.125123401;
PCHf[1][2] = -0.298905246;
PCHf[2][0] = -0.122042146;
PCHf[2][1] = -0.300529172;
PCHf[3][0] = -0.307584705;
```

A.8 Spine Coefficients

```
for (i = 3; i < 10; i++) piCCf[0][0][i] = 0.0049586079;
piCCf[1][0][1] = 0.021693495;
piCCf[0][1][1] = 0.021693495;
for (i = 2; i < 10; i++) piCCf[1][0][i] = 0.0049586079;
for (i = 2; i < 10; i++) piCCf[0][1][i] = 0.0049586079;
piCCf[1][1][2] = -0.002088750;
for (i = 3; i < 10; i++) piCCf[1][1][i] = -0.00804280;
piCCf[2][0][1] = 0.024698831850;
piCCf[0][2][1] = 0.024698831850;
piCCf[2][0][2] = -0.00597133450;
piCCf[0][2][2] = -0.00597133450;
for (i = 3; i < 10; i++) piCCf[2][0][i] = 0.0049586079;
for (i = 3; i < 10; i++) piCCf[0][2][i] = 0.0049586079;
piCCf[2][1][1] = 0.00482478490;
piCCf[1][2][1] = 0.00482478490;
piCCf[2][1][4] = -0.01168893870;
piCCf[1][2][4] = -0.01168893870;
piCCf[2][1][5] = -0.013377877400;
piCCf[1][2][5] = -0.013377877400;
piCCf[2][1][6] = -0.015066816000;
piCCf[1][2][6] = -0.015066816000;
for (i = 7; i < 10; i++) piCCf[2][1][i] = -0.015066816000;
for (i = 7; i < 10; i++) piCCf[1][2][i] = -0.015066816000;
piCCf[2][2][1] = 0.0472247850;
piCCf[2][2][3] = 0.0198529350;
piCCf[2][2][4] = 0.01654411250;
piCCf[2][2][5] = 0.013235290;
piCCf[2][2][6] = 0.00992646749999 ;
piCCf[2][2][7] = 0.006617644999;
```

```
  piCCf[2][2][8] = 0.00330882250;
  piCCf[3][0][1] = -0.05989946750;
  piCCf[0][3][1] = -0.05989946750;
  piCCf[3][0][2] = -0.05989946750;
  piCCf[0][3][2] = -0.05989946750;
  for (i = 3; i < 10; i++) piCCf[3][0][i] = 0.0049586079;
  for (i = 3; i < 10; i++) piCCf[0][3][i] = 0.0049586079;
  piCCf[3][1][2] = -0.0624183760;
  piCCf[1][3][2] = -0.0624183760;
  for (i = 3; i < 10; i++) piCCf[3][1][i] = -0.0624183760;
  for (i = 3; i < 10; i++) piCCf[1][3][i] = -0.0624183760;
  piCCf[3][2][1] = -0.02235469150;
  piCCf[2][3][1] = -0.02235469150;
  for (i = 2; i < 10; i++) piCCf[3][2][i] = -0.02235469150;
  for (i = 2; i < 10; i++) piCCf[2][3][i] = -0.02235469150;
  for (i = 2; i < 10; i++) piCCdfdx[2][3][i] = 0.0624183760;
  for (i = 2; i < 10; i++) piCCdfdy[3][2][i] = 0.0624183760;
  piCCdfdz[2][1][4] = -0.0100220;
  piCCdfdz[1][2][4] = -0.0100220;
  piCCdfdz[2][1][5] = -0.0100220;
  piCCdfdz[1][2][5] = -0.0100220;
  for (i = 4; i < 10; i++) piCCdfdz[2][2][i] = -0.0033090;
```

A.9 Revisions

```
//  make top end flat instead of zero piCC


  i = 3;
  z = 4;
```

```
  for (j = 0; j < 4; j++)
      for (k = 1; k < 10; k++)
          piCCf[z][j][k] = piCCf[i][j][k];



  for (i = 0; i < 4; i++)
      for (j = i+1; j < 5; j++)
          for (k = 1; k < 10; k++)
              piCCf[i][j][k] = piCCf[j][i][k];




  for (k = 1; k < 10; k++) piCCf[4][4][k] = piCCf[3][4][k];
  z = 10;
  k = 9;
  for (i = 0; i < 5; i++)
      for (j = 0; j < 5; j++)
      piCCf[i][j][z] = piCCf[i][j][k];




//  make top end flat instead of zero piCH

  i = 3;
  z = 4;
  for (j = 0; j < 4; j++)
      for (k = 1; k < 10; k++)
          piCHf[z][j][k] = piCHf[i][j][k];
```

```
for (i = 0; i < 4; i++)
    for (j = i+1; j < 5; j++)
        for (k = 1; k < 10; k++)
            piCHf[i][j][k] = piCHf[j][i][k];




for (k = 1; k < 10; k++) piCHf[4][4][k] = piCHf[3][4][k];
z = 10;
k = 9;
for (i = 0; i < 5; i++)
    for (j = 0; j < 5; j++)
    piCHf[i][j][z] = piCHf[i][j][k];
```

A.10 Implementation of Smooth LJ Cutoff Function

```
declare and initialize variables
double vdw,slw,dvdw,dslw,drij,swidth,tee,tee2;
double rljmin,rljmax,sigcut,sigmin,sigwid;


      sigwid = 0.84;
      sigcut = 3.0;
      sigmin = sigcut - sigwid;


      rljmin = sigma[itype][jtype];!       rljmax = sigcut * rljmin;
      rljmin = sigmin * rljmin;
```

```
if (rij > rljmax)
   slw = 0.0;
   dslw = 0.0;
else if (rij > rljmin)
   drij = rij - rljmin;
   swidth = rljmax - rljmin;
   tee = drij / swidth;
   tee2 = pow (tee,2);
   slw = 1.0 - tee2 * (3.0 - 2.0 * tee);
   dslw = 6.0 * tee * (1.0 - tee) / rij / swidth;

else
   slw = 1.0;
   dslw = 0.0;

 r2inv = 1.0/rijsq;
 r6inv = r2inv*r2inv*r2inv;

vdw = r6inv*(lj3[itype][jtype]*r6invlj4[itype][jtype]);
dvdw = -r6inv * (lj1[itype][jtype]*r6inv - lj2[itype][jtype]) / rij;

// VLJ now becomes vdw * slw, derivaties, etc.

VLJ = vdw * slw;
dVLJ = dvdw * slw + vdw * dslw;

 Str = Sp2(rij,rcLJmin[itype][jtype],rcLJmax[itype][jtype],dStr);
 VA = Str*cij*VLJ;
```

A.11 P_{ij} Bounds

```
for (i = 0; i < (int) piCHdom[0][1]; i++)
      for (j = 0; j < (int) piCHdom[1][1]; j++)
        for (k = 0; k < (int) piCHdom[2][1]; k++)
          for (l = 0; l < 64; l = l+1)
            fgets(s,MAXLINE,fp);
            sscanf(s,"%lg",&piCH[i][j][k][l]);
```

A.12 N_{ij}, N_{ji}, and N_{ij}^{conj} Bounds

```
if (typei==0 && typej==0)
    if (Nij<piCCdom[0][0]) Nij=piCCdom[0][0];
    if (Nij>piCCdom[0][1]) Nij=piCCdom[0][1];
    if (Nji<piCCdom[1][0]) Nji=piCCdom[1][0];
    if (Nji>piCCdom[1][1]) Nji=piCCdom[1][1];
    if (Nijconj<piCCdom[2][0]) Nijconj=piCCdom[2][0];
    if (Nijconj>piCCdom[2][1]) Nijconj=piCCdom[2][1];


if (typei==0 && typej==1 || typei==1 && tyej==0)
      if (Nij<piCHdom[0][0]) Nij=piCHdom[0][0];
      if (Nij>piCHdom[0][1]) Nij=piCHdom[0][1];
      if (Nji<piCHdom[1][0]) Nji=piCHdom[1][0];
      if (Nji>piCHdom[1][1]) Nji=piCHdom[1][1];
      if (Nijconj<piCHdom[2][0]) Nijconj=piCHdom[2][0];
      if (Nijconj>piCHdom[2][1]) Nijconj=piCHdom[2][1];
```

A.13 P_{ij} Types

```
if (typei == 0 && typej == 1) [NOTE:  Changed from if (!(typei == typej))
if (NijC < pCHdom[0][0]) NijC=pCHdom[0][0];
      if (NijC > pCHdom[0][1]) NijC=pCHdom[0][1];
      if (NijH < pCHdom[0][0]) NijH=pCHdom[1][0];
      if (NijH > pCHdom[1][1]) NijH=pCHdom[1][1];
    if (fabs(NijC-floor(NijC)) < TOL && fabs(NijH-floor(NijH)) < TOL)
      Pij = PCHf[(int) NijC][(int) NijH];
      dN2[0] = PCHdfdx[(int) NijC][(int) NijH];
      dN2[1] = PCHdfdy[(int) NijC][(int) NijH];
      done = 1;

    if (done == 0)
      x = (int) (floor(NijC));
      y = (int) (floor(NijH));
      for (i = 0; i<16; i++) coeffs[i] = pCH[x][y][i];
      Pij = Spbicubic(NijC,NijH,coeffs,dN2);



  if (typei == 1 && typej == 0)
    Pij = 0.0;
    dN2[0] = 0.0;
    dN2[1] = 0.0;
```

Bibliography

[1] B. J. Alder and T. Wainwright, "Velocity autocorrelations for hard spheres," *Phys. Rev. Lett.*, vol. 18, 1967.

[2] J. Pople, J. Mclver, and N. Ostlund, "Finite pertubration theory for nuclear spin coupling constants," *J. Chem. Phys.*, vol. 1, pp. 465–466, 1967.

[3] B. Alder and T. Wainwright, "Studies in molecular dynamics i. general method," *J. Chem. Phys.*, vol. 31, p. 459, 1959.

[4] A. Pigarov, P. Krstic, S. Krasheninnikov, R. Doerner, and T. Rognlien, "Dynamis models for plasma-wall interactions," *Contrib. Plasma Phys.*, vol. 52, pp. 465–477, 2012.

[5] M. Buhl and G. Wipiff, "Insights into uranyl chemistry from molecular dynamics simulations," *ChemPChem*, vol. 12, pp. 3095–3105, 2011.

[6] F. Zheng and C. Zhang, "Computational modeling of solven effects on protein-ligand interactions using fully polarizable continuum model and rational drug design," *Comm. in Comp. Phys.*, vol. 13, pp. 31–60, 2012.

[7] O. Kwon, J. Lee, J. Park, K. Kim, and J. Kang, "Molecular dynamics simulation study on graphene-nanoribbion-resonators tuned by adjusting axial strain," *Curr. App. Phys.*, vol. 13, pp. 360–365, 2012.

[8] D. W. Brenner, O. A. Shenderova, J. A. Harrison, S. J. Stuart, B. Ni, and S. B. Sinnot, "A second-generation reactive empirircal bond order (REBO) potential energy expression for hydrocarbons," *J. Phys.: Condens. Matter*, vol. 14, pp. 783–802, 2002.

[9] S. J. Stuart, A. B. Tutein, and J. A. Harrison, "A reactive potential for hydrocarbons with intermolecular interactions," *J. Chem. Phys.*, vol. 112, pp. 6472–6486, 2000.

[10] J. W. Gibbs, *Elementary Principles in Statistical Mechanics*. New York: C. Scribner, 1902.

[11] J. Westerhout, D. Borodin, R. S. Al, S. Brezinsek, M. H. J. Hoen, A. Kirschner, S. Lisgo, H. J. van Meiden, V. Philipps, M. J. van de Pol, A. E. Shumack, G. D. Temmerman, W. A. J. Vijvers, G. M. Wright, N. J. L. Cardozo, J. Rapp, and G. J. van Rooji, "Chemical erosion of different carbon composits under iter-relevant plasma conditions," *Phys. Scr.*, vol. T138, p. 014017, 2009.

[12] H. Zhang and F. Meyer, "Steady-state and transient hydrocarbon procution in graphite by low energy impact of atomic and molecular deuterium projectiles," *J. Nuc. Mat.*, vol. 390, pp. 127–131, 2009.

[13] Y. Ueda, T. Sugai, Y. Ohtsuka, and M. Nishikawa, "Mechanism of chemical sputtering of graphite under high flux deuterium bombardment," *J. Nuc. Mat.*, vol. 282, pp. 216–232, 2000.

[14] P. H. Hunenberger, "Thermostat algorithms for molecular dynamics simulations," *Adv. Poly. Sci.*, vol. 173, pp. 105–149, 2005.

[15] S. J. Stuart, M. Fallet, P. S. Krstic, and C. O. Reinhold, "Evolution of carbon surfaces under simulated bombardment by deuterium," *J. Phys.: Conf. Series*, vol. 194, p. 012059, 2009.

[16] M. Fallet and S. J. Stuart, "Evolution of carbon based surfaces under bombardment: Examining the steady-state surface properties and the effect of potential," *Nucl. Instr. Meth. Phys. Res. B*, vol. 269, pp. 1271–1275, 2011.

[17] S. A. Adelman and J. D. Doll, "Generalized langevin equation approach for atom/solid surface scattering: General formulation for classical scattering off harmonic solids.," *J. Chem. Phys.*, vol. 64, pp. 2376 – 2388, 1976.

[18] L. Verlet, "Computer "experiments" on classical fluids. I. Thermodynamical properties of Lennard-Jones molecules," *Phys. Rev.*, vol. 159, pp. 98–103, 1967.

[19] J. Slater and G. Koster, "Simplified lcao method for the periodic potential problem," *Phys. Rev.*, vol. 94, pp. 1498–1524, 1954.

[20] P. Morse, "Diatomic molecules according to the wave mechanics ii. vibrational levels," *Phys. Rev.*, vol. 34, pp. 57–64, 1929.

[21] D. Harringt, "Separable potentials and coulomb interactions," *Phys. Rev.*, vol. 139, p. B691, 1965.

[22] J. Tersoff, "Modeling solid-state chemistry: Interatomic potentials for multicomponent systems," *Phys. Rev. B*, vol. 39, pp. 5566–5568, 1989.

[23] J. Tersoff, "New empirical model for the structural properties of silicon," *Phys. Rev. Lett.*, vol. 56, pp. 632–635, 1986.

[24] Y. Richenko, O. Marchuk, W. Biel, T. Schlummer, D. Schultz, and E. Stambulchik, "A non-statistical atomic model for beam emission and motional stark effect in fusion plasmas," *Rev. of Sci. Instr.*, vol. 83, p. D504, 2012.

[25] W. Jacob, C. Hopf, and M. Schluter, "Chemical sputtering of carbon materials due to combined bombardment of ions and atomic hydrogen," *Phys. Scr.*, vol. T124, pp. 32–36, 2006.

[26] F. Meyer, H. Zhang, L. Vergara, and H. Krause, "Chemical sputtering of room temperature atj graphite and hopg by slow atomic and molecular d ions," *Nucl. Instr. Meth. Phys. Res. B*, vol. 258, pp. 264–269, 2007.

[27] H. Zhang, F. Meyer, H. Meyer, and M. Lance, "Surface modification and chemical sputtering of graphite induced by low-energy atomic and molecular deuterium ions," *Vacuum*, vol. 82, pp. 1285–1290, 2008.

[28] J. Roth, J. Bohdansky, W. Poschenrieder, and M. Sinha, "Physical and chemical sputtering of graphite and sic by hydrogen and helium in the energy range of 600 to 7500 ev," *J. Nuc. Mat.*, vol. 63, pp. 222–229, 1976.

[29] E. D. Rooji, U. von Toussaint, A. W. Kleyn, and W. J. Goedheer, "Molecular dynamics simulations of amorphous hydrogenated carbon under high hydrogen fluxes," *Phys. Chem. Chem. Phys.*, vol. 11, pp. 9823–9830, 2009.

[30] F. W. Meyer, P. S. Krstic, L. I. Vergara, H. Krause, C. O. Reinhold, and S. J. Stuart, "Low energy chemical sputtering of ATJ graphite by atomic and molecular deuterium ions," *Phys. Scr.*, vol. T128, pp. 50–54, 2007.

[31] B. N. Jariwala, C. V. Ciobanu, and S. Agarwal, "Atomic hydrogen interactions with amorphous carbon thin films," *J. Appl. Phys.*, vol. 106, p. 073305, 2009.

[32] E. Hollmann, P. Krstic, R. Doerner, D. Nishjima, A. Y. Pigarov, C. Reinhold, and S. Stuart, "Measurement and modeling of hydrogen molecule rovibrational accomodation on e-294 polycrystalline graphite," *Plasma. Phys. Control. Fusion*, vol. 50, p. 102001, 2008.

[33] P. Krstic, E. Hollmann, C. Reinhold, S. Stuart, R. Doerner, D. Nishijima, and A. Y. Pigarov, "Transfer or rovibrational energies in hydrogen plasma-carbon surface interactions," *J. Nuc. Mat.*, vol. 390, pp. 88–91, 2009.

[34] P. S. Krstic, C. O. Reinhold, and S. J. Stuart, "Energy and angle specra of sputtered particles for low-energy deuterium impact of deuterated amorphous carbon," *J. Appl. Phys.*, vol. 104, p. 103308, 2008.

[35] C. Reinhold, P. Krstic, and S. Stuart, "Time scales of chemical sputtering of carbon," *Nucl. Instr. Meth. Phys. Res. B*, vol. 258, pp. 274–277, 2007.

[36] C. Reinhold, P. Krstic, S. Stuart, H. Zhang, P. Harris, and F. Meyer, "Isotope dependence of chemical erosion of carbon," *J. Nuc. Mat.*, vol. 401, pp. 1–12, 2010.

[37] F. Meyer, H. Zhang, M. Lance, and H. Krause, "Chemical sputtering and surface damage of graphite by low-energy atomic and molecular hydrogen and deuterium parojectiles," *Vacuum*, vol. 82, pp. 880–887, 2008.

[38] M. Balden and J. Roth, "New weight-loss measurements of the chemical erosion yields of carbon materials under hydrogen ion bombardment," *J. Nuc. Mat.*, vol. 280, pp. 39–44, 2000.

[39] C. Reinhold, P. Krstic, and S. Stuart, "Hydrogen reflection in low-energy collisions with amorphous carbon," *Nucl. Instr. Meth. Phys. Res. B*, vol. 267, pp. 691–694, 2009.

[40] K. D. Krantzman, Z. Postawa, B. J. Garrison, N. Winograd, S. J. Stuart, and J. A. Harrison, "Understanding colliision cascades in molecular solids," *Nucl. Instr. Meth. Phys. Res. B*, vol. 180, pp. 159–163, 2001.

[41] P. S. Krstic, C. O. Reinhold, and S. J. Stuart, "Chemical sputtering by impact of excited molecules," *Europhys. Lett.*, vol. 77, p. 33002, 2007.

[42] P. Krstic, C. Reinhold, and S. Stuart, "Plasma-surface interactions of hydrogenated carbon," *Nucl. Instr. Meth. Phys. Res. B*, vol. 267, pp. 704–710, 2009.

[43] G. Federici and C. H. Wu, "Modelling of the interaction of hydrogen plasma with amorphous carbon films redepositied in fusion devices," *J. Nuc. Mat.*, vol. 207, pp. 62–85, 1993.

[44] T.-B. Ma, Y.-Z. Hu, and H. Wang, "Molecular dynamics simulation of sheer-induced graphitization of amorphous carbon films," *Carbon*, vol. 47, pp. 1953–1957, 2009.

[45] C. Hopf and W. Jacob, "Bombardment of graphite with hydrogen isotopes: A model for the energy dependence of the chemical sputtering yield," *J. Nuc. Mat.*, vol. 342, pp. 141–147, 2005.

[46] S. J. Stuart, P. S. Krstic, T. Embry, and C. O. Reinhold, "Methane production by deuterium impact at carbon surfaces," *Nucl. Instr. Meth. Phys. Res. B*, vol. 255, pp. 202–207, 2007.

[47] A. Ito and H. Nakamura, "Molecular dynamics simulation of collisions between hydrogen and graphite," *J. Plasma Phys.*, vol. 72, pp. 805–808, 2006.

[48] H. Nakamura and A. Ito, "Molecular dynamics simulation of sputtering process of hydrogen and graphene sheets," *Mol. Sim.*, vol. 33, pp. 121–126, 2006.

[49] A. Ito and H. Nakamura, "Molecular dynamics simulation of bombardment of hydrogen atoms on graphite surface," *Comm. in Comp. Phys.*, vol. 4, pp. 592–610, 2008.

[50] W. Jacob and J. Roth, *Chemical sputtering.* Topics in Applied Physics, Springer, 2007.

[51] M. Schluter, C. Hopf, T. Schwarz-Selinger, and W. Jacob, "Temperature dependence of the chemical sputtering of amorphous hydrogenated carbon films by hydrogen," *J. Nuc. Mat.*, vol. 376, pp. 33–37, 2008.

[52] F. Meyer, H. Zhang, L. Vegara, and H. Krause, "Chemical sputtering of room temperature atj graphite and hopg by slow atomic and molecular d ions," *Nucl. Instr. Meth. Phys. Res. B*, vol. 258, pp. 264–269, 2007.

[53] L. I. Vergara, F. W. Meyer, H. F. Krause, P. Traskelin, K. Nordlund, and E. Salonen, "Methane production from ATJ graphite by slow atomic and molecular d ions: Evidence for projectile molecule-size-dependent yields at low energies," *J. Nucl. Mater.*, vol. 357, pp. 9–18, 2006.

[54] F. W. Meyer, P. S. Krstic, L. I. Vergara, H. F. Krause, C. O. Reinhold, and S. J. Stuart, "Low energy chemical sputtering of ATJ graphite by atomic and molecular d ions," *Physica Scripta*, vol. T128, pp. 50–54, 2007.

[55] E. M. Hollman, P. S. Krstic, R. P. Doerner, D. Nishijima, A. Y. Pigarov, C. O. Reinhold, and S. J. Stuart, "Measurement and modeling of hydrogen molecule ro-vibrational accomodation on E-294 polycrystalline graphite," *Plasma Phys. Control. Fusion*, vol. 50, p. 102001, 2008.

[56] E. Salonen, K. Nordlund, J. Keinonen, and C. Wu, "Swift chemical sputtering of amorphous hydrogenated carbon," *Phys. Rev. B*, vol. 63, p. 195415, 2001.

[57] J. Marian, L. A. Zepeda-Ruiz, N. Couto, E. M. Bringa, G. H. Gilmer, P. C. Stangeby, and T. D. Rognlien, "Characterization of sputtering products during graphite exposure to deuterium ions by molecular dynamics," *J. Appl. Phys.*, vol. 101, p. 044506, 2007.

[58] P. S. Krstic, S. J. Stuart, and C. O. Reinhold, "Chemical sputtering of fusion plasma-facing carbon surfaces," *AIP Conference Proceedings*, vol. 876, pp. 201–208, 2006.

[59] P. S. Krstic, C. O. Reinhold, and S. J. Stuart, "Chemical sputtering from amorphous carbon under sputtering by deuterium atoms and molecules," *New J. Phys.*, vol. 9, p. 209, 2007.

[60] S. J. Stuart, P. S. Krstic, T. A. Embry, and C. O. Reinhold, "Methane production by deuterium impact at carbon surfaces," *Nucl. Instr. Meth. Phys. Res. B*, vol. 255, pp. 202–207, 2007.

[61] A. Ito, Y. Wang, S. Irle, K. Morokuma, and H. Nakamura, "Molecular dynamics simulation of hydrogen atom sputtering on the surface of graphite with defect and edge," *J. Nucl. Mater.*, vol. 390-391, pp. 183–187, 2009.

[62] D. W. Brenner, "Empirical potential for hydrocarbons for use in simulating the chemical vapor deposition of diamond films," *Phys. Rev. B*, vol. 42, pp. 9458–9471, 1990.

[63] D. W. Brenner, O. A. Shenderova, J. A. Harrison, S. J. Stuart, B. Ni, and S. Sinnott, "A second-generation reactive empirical bond order (REBO) potential energy expression for hydrocarbons," *J. Phys.: Condens. Matter*, vol. 14, pp. 783–802, 2002.

[64] S. J. Stuart, J. M. Hicks, and M. T. Mury, "An iterative variable-timestep algorithm for molecular dynamics simulations," *Mol. Sim.*, vol. 29, pp. 177–186, 2003.

[65] J. Roth, B. M. U. Scherzer, R. S. Blewer, D. K. Brice, S. T. Pieraux, and W. R. Wampler, "Trapping, detrapping and replacement of kev hydrogen implanted into graphite," *J. Nucl. Mater.*, vol. 93-94, pp. 601–607, 1980.

[66] M. Baldwin and R. Doerner, "Helium induced nanoscopic morphology on tungsten under fusion relevant plamsa conditions," *Nuc. Fus.*, vol. 48, p. 035001, 2008.

[67] S. Uhlmanna, T. Frauenheim, and Y. Lifshitz, "Molecular dynamics study of the fundamental processes involved in subplantation of diamondlike carbon," *Phys. Rev. Lett.*, vol. 81, pp. 641–644, 1998.

[68] A. Ito, Y. Wang, S. Irle, K. Morokuma, and H. Nakamura, "Molecular dynamics simulation of hydrogen atom sputtering on the surface of graphite wi th defect and edge," *J. Nuc. Mat.*, vol. 390, pp. 183–187, 2009.

[69] P. Krstic, C. Reinhold, and S. Stuart, "Chemical sputtering from amorphous carbon under bombardment by deuterium atoms and molecules," *New J. Phys.*, vol. 9, p. 1367, 2007.

[70] R. Ning, Y. Li, W. Zhou, Z. Zheng, and X. Ju, "Modeling d retention in w under d ions and neutrons irradiation," *J. Nuc. Mat.*, vol. 430, pp. 20–26, 2012.

[71] A. Backer, P. Lhullier, C. Becquart, and M. Barthe, "Modeling of the implanation and the annealing stages of 800 kev he-3 implanted tungsten: Formation of nanovoids in thenear surface region," *J. Nuc. Mat.*, vol. 429, pp. 78–91, 2012.

[72] J. Marian and T. Hoang, "Modeling fast nuetron irradiation damage accumulated in tungsten," *J. Nuc. Mat.*, vol. 429, pp. 293–297, 2012.

[73] E. Stolyarova, D. Stolyarov, K. Bolotin, and S. R. et. al., "Observation of graphene bubbles and effective mass transport under graphene films," *Nano Lett.*, pp. 332–337, 2009.

[74] J. Zabel, R. R. Nair, A. Ott, T. Georgiou, G. Andre K, K. S. Novoselov, and C. Casiraghi, "Raman spectroscopy of graphite and bilyar under biaxial strain: Bubbles and balloons," *Nano Lett.*, vol. 12, pp. 617–621, 2011.

[75] S. Winder and J. Bender, "Precipitation and delamination of crystalline graphite bubbles from molten iron, nickel, and cobalt by splat cooling," *Carbon*, vol. 46, pp. 940–948, 2008.

[76] I. Aleksandrov, A. Gonchiov, E. Yakovenko, and s.M Stishov, *High Pressure Study of Diamond, Graphite, and Related Materials*. Washington, D.C.: Terrapub, 1992.

[77] T. Mattson, J. Lane, D. K. Cochrane, M. Desjarais, A. T. amd F. Pierce, and G. Great, "First-princoples and classical molecular dynamics simulation of shoked polymers," *Phys. Rev. B*, vol. 81, p. 054103, 2010.

[78] C. Heusch, H.-G. Moser, and A. Kholodenko, "Direct measurements of the thermal conductivity of various pyrolytic graphite samples (pg, tpg) used as thermal dissipation agents in detector applications," *Nucl. Instr. Meth. Phys. Res. A*, vol. 480, pp. 463–469, 2002.